Mineralogical transformations set slow weathering rates in low-porosity metamorphic bedrock on mountain slopes in a tropical climate

Ricarda Behrens[1,2,*], Julien Bouchez[1,3], Jan A. Schuessler[1], Stefan Dultz[4], Tilak Hewawasam[5], Friedhelm von Blanckenburg[1]

[1]GFZ German Research Centre for Geosciences, Section 3.4 Earth Surface Geochemistry, Telegrafenberg, 14473 Potsdam, Germany

[2]Deutsche Forschungsgemeinschaft (DFG) Graduate School 1364, University of Potsdam, Institute of Geosciences, Karl-Liebknecht Str. 24, Haus 27, 14476 Potsdam, Germany

[3]Institut de Physique du Globe de Paris, Université Paris Diderot, Sorbonne Paris-Cité, Centre National de la Recherche Scientifique, 1 rue Jussieu, 75238 Paris cedex 05, France

[4]Institute of Soil Science, Leibniz Universität Hannover, Herrenhäuser Str. 2, 30419 Hannover, Germany

[5]Department of Geography, University of Peradeniya, Peradeniya, Sri Lanka

*corresponding author: rimaek@gfz-potsdam.de

Abstract

In the Sri Lankan Highlands erosion and chemical weathering rates are among the lowest for global mountain denudation. In this tropical humid setting, highly weathered deep saprolite profiles have developed from high-grade metamorphic charnockite during spheroidal weathering of the bedrock. The spheroidal weathering produces rounded corestones and spalled rindlets at the rock-saprolite interface. We used detailed textural, mineralogical and chemical analyses to reconstruct the sequence of weathering reactions and their causes. The first mineral attacked by weathering was found to be pyroxene initiated by *in situ* Fe oxidation. Volumetric calculations suggest that this oxidation leads to the generation of porosity due to the formation of micro-fractures allowing for fluid transport and subsequent dissolution of biotite and plagioclase. The rapid ensuing plagioclase weathering leads to formation of high secondary porosity in the corestone over a distance of only a few cm and eventually to the final disaggregation of bedrock to saprolite. The first secondary phases are oxides or amorphous precipitates from which secondary minerals (mainly gibbsite, kaolinite and goethite) form. As oxidation is the first weathering reaction, the supply of O_2 is a rate-limiting factor for chemical weathering. Hence, the supply of O_2 and its consumption at depth connects processes at the weathering front with those at the Earth's surface in a feedback mechanism. The strength of the feedback depends on the relative weight of advective *versus* diffusive transport of O_2 through the weathering profile. The feedback will be stronger with dominating diffusive transport. The low weathering rate is explained by the nature of this feedback that is ultimately dependent on the transport of O_2 through the whole regolith, and on lithological factors such as low bedrock porosity and the amount of Fe-bearing primary minerals. Tectonic quiescence in this region and low pre-development erosion rate (attributed

to a dense vegetation cover) minimize the rejuvenation of the thick and cohesive regolith column, finally leading to low denudation rates.

1 Introduction

The fact that most of the continental areas are covered by regolith (composed of the mobile soil layer overlying the *in situ* weathered saprolite) suggests that over millennial time scales removal of regolith material by erosion is mostly balanced by its production through bedrock weathering. This observation hints at the existence of a feedback between regolith depth and rates of weathering and erosion processes that produce and destroy regolith, respectively (Carson and Kirkby, 1972; Heimsath et al., 1997). The existence of this feedback is also suggested by the empirical negative relationship between soil production and soil thickness, the so-called "soil production function" (*e.g.*, Heimsath et al., 1997; Heimsath et al., 2009). The "soil production function" has been established for the mobile soil layer. Models for regolith development have suggested that this relationship might extend through the entire regolith (Lebedeva et al., 2010). The fact that a negative feedback between regolith thickness and weathering rate exists is an implicit conclusion of the observation that weathering rates are generally low where thick regolith prevails – a phenomenon commonly lumped into the term "soil shielding" (Goddéris et al., 2008; Hartmann et al., 2014; Stallard, 1995). However, alternative views suggest that in tectonically quiescent cratons, this feedback is absent such that regolith production outpaces erosion, leading to continuously thickening weathering profiles (Lebedeva et al., 2010).

In order to develop an improved understanding of the mechanisms leading to these relationships, it is critical (i) to examine in detail the mineralogical transformations occurring at the "weathering front", where rock is first converted into saprolite; (ii) to identify the reactive phases (O_2, protons, acids, complexing agents) that limit the rate of these mineralogical transformations; and (iii) to characterize the formation of pathways, such as fractures and macro-cracks or connected pore spaces that support transport of reactive phases to the weathering front. In particular, an oxidative process for spheroidal fracturing was proposed by Buss et al. (2008), Fletcher et al. (2006), and Lebedeva et al. (2007), where Fe(II) in bedrock minerals is oxidized after O_2 transport from the soil surface into the rock. Oxidative weathering produces a specific volume increase of the solid material and thus builds up strain that fractures the rock. Similarly, precipitation of secondary clay minerals following dissolution of primary minerals was also proposed to result in strain build-up and rock fracturing (Jamtveit et al., 2011; Jamtveit et al., 2008; Røyne et al., 2008; Rudge et al., 2010). In contrast to pathways that require the generation of strain, the access of reactive phases from the surface to the weathering front might also be promoted by the formation of secondary porosity by primary mineral dissolution and precipitation of secondary minerals with a lower molar volume (Lebedeva et al., 2007; Navarre-Sitchler et al., 2011; Sak et al., 2010; Velbel, 1993). All these models imply that the supply of a reactive compound from the atmosphere (*e.g.*, O_2) or from the upper regolith layers (*e.g.*, organic acids) is necessary to the

downward propagation of the weathering front, thereby providing a negative feedback between the regolith thickness and mineral dissolution taking place at depth (Fletcher et al., 2006). Alternative models suggest that the lowering of the water table induced by channel incision promotes the downward propagation of the weathering front (Edmond et al., 1995; Rempe and Dietrich, 2014). Such a mechanism also requires the formation of fractures and open pore spaces for corrosive fluids to reach unweathered minerals in low-porosity bedrock. Evidence is still lacking about the processes that generate these fluid pathways and about their relative contribution to the weathering front advance.

Exploring the way these pathways are generated is important because their understanding is fundamental to quantitative models of the weathering front advance (Bazilevskaya et al., 2013, 2015; Brantley et al., 2008; Fletcher et al., 2006; Goddéris et al., 2006; Lebedeva et al., 2007; Lebedeva et al., 2010; Moore et al., 2012; Navarre-Sitchler et al., 2011). These models essentially characterize the transport of solutes and gases through regolith profiles and the participating weathering reactions. The successful application of these models relies on an accurate knowledge of the weathering system's transport properties (*e.g.*, soil and saprolite permeability) and chemical parameters (*e.g.*, kinetics of dissolution and precipitation, or equilibrium constants). The nature and properties of the secondary precipitates forming during weathering (*i.e.*, their mineralogy, crystallinity, or ability to form aggregates) exert a strong control on the outputs of such models (Maher et al., 2009). In particular, many weathering reactions have been reported to produce amorphous intermediate phases rather than forming crystalline clays directly from primary minerals (Chadwick and Chorover, 2001; Dahlgren et al., 1997; Hellmann et al., 2012; Steefel and van Cappellen, 1990). Hence, the relevance of these weathering model predictions needs to be evaluated against thorough field observations across a range of different lithological and geomorphological contexts.

A weathering profile at Hakgala in the Central Highlands of Sri Lanka offers the opportunity to explore in detail the sequence of weathering processes from coherent bedrock to loose soil in a tropical mountain environment that is not currently subject to significant tectonic activity. Weathering and erosion rates, and the degree of chemical weathering have been quantified in great detail (Gunnell and Louchet, 2000; Hewawasam et al., 2013; Hewawasam et al., 2003; Vanacker et al., 2007b; von Blanckenburg et al., 2004), providing boundary conditions on the relevant mass fluxes across the weathering system. Hewawasam et al. (2013) showed that in this setting weathering along hill slopes is slow, and operates at a steady state, *i.e.*, regolith removal by erosion balances regolith production by downward propagation of the weathering front. Such steady state is indicated by finding roughly similar weathering rates over two different time scales. The rates calculated from river dissolved loads (time scale ca. 10 years) agree with those from cosmogenic nuclides that are combined with chemical weathering indices in the profile (time scale ca. 10^4 years). Because the Hakgala weathering profile is a well-characterized, thick regolith profile representative of slow denudation-tropical settings that prevail on a large portion of the continental surface (Braun et al., 2009; Braun et al., 2012; Dequincey et al., 1999; Edmond et al., 1995; Hewawasam et al., 2013), it provides a perfect field site to study in

detail the links between regolith properties and weathering at depth. In particular, the Hakgala weathering profile features corestones consisting of bedrock fragments remaining in the regolith that are progressively spheroidally weathered. As such, corestones include a core of bedrock and several layers around this core with increasing weathering intensities outward. They serve as small natural laboratories on which incipient weathering can be studied in detail (Buss et al., 2008; Ma et al., 2012; Sak et al., 2004; Sak et al., 2010). In fact, as the fronts of the respective weathering reactions move inwards with time, the spatial alignment also represents the state of weathering at different times, with outer layers having been exposed to weathering for longer times than inner layers.

In the present study, we build upon chemical and mineralogical analyses conducted by Hewawasam et al. (2013) who derived chemical mass fluxes, weathering degree, and the weathering front advance rate. Here, we further (i) identify the chemical reaction mechanisms and show the significance of amorphous secondary phases for the conversion of bedrock to loose material; (ii) identify textural changes between the compartments of the weathering profile; and (iii) discuss reactions that involve element fluxes and volume changes driving chemical weathering and the nature of the feedbacks between regolith thickness and propagation of the weathering front. With these new results we address the following questions: What are the mechanisms responsible for the slow propagation of the weathering front in deep regoliths under tropical climate? How is the propagation rate of the weathering front influenced by regolith transport properties? Why are low weathering rates in tropical mountain regions often associated with a thick regolith cover?

2. Study site and analytical methods

2.1 Study site and sampling

The Hakgala weathering profile (06.92923° N, 80.81834° E) is located on a fresh road cut on the road from Nuwara Elia to Welimada in the Central Highlands of Sri Lanka (please see figure 1, p. 204 in Hewawasam et al., 2013). The site is exposed to two monsoon seasons, mean annual precipitation is 5000 mm, and mean annual temperature is 20 °C. The vegetation is comprised of upper montane rainforest. An approximately 10 m-thick regolith profile (including a zone with corestones at the bottom, a deeply weathered saprolite layer, and 60 cm of soil on top, Figure 1A) developed over a charnockitic bedrock lithology, with plagioclase (An25), K-feldspar, and quartz as major mineral components and minor amounts of biotite and orthopyroxene. The weathering of the bedrock is initiated along large conjugated fractures dividing the bedrock into blocks. The separated blocks of charnockite weather spheroidally resulting in a transition zone featuring rounded corestones between coherent bedrock and deeply weathered saprolite. Due to the inward advance of weathering, corestones are surrounded by spheroidally spalled “rindlets” (Buss et al., 2008). These spheroidally weathered corestones feature several weathering fronts on a cm- to dm-scale, separating a virtually unweathered core from saprolite-like material in the outer rindlets. Despite humid, tropical climate and

high relief the chemical weathering (chemically removed material) and total denudation (sum of chemical weathering and physical erosion) rates were calculated to be as low as 22 t km^{-2} y^{-1} and 42 t km^{-2} y^{-1}, respectively (Hewawasam et al., 2013).

Samples from the profile (Figure 1A) were taken in October 2010 from the bedrock to the soil layer (Hewawasam et al., 2013). A corestone was sampled and visually divided into several zones of different weathering degree, which were then characterized microscopically and chemically by Hewawasam et al. (2013). These different corestone zones are (Figure 1B): the dark, visually unweathered core, termed zone 1; a light gray layer surrounding the core, termed zone 2; a yellow rim, termed zone 3; and successive "rindlets", termed zone 4 (4a and 4c were studied in the present contribution). The saprolite itself is highly weathered, as half of the mass of the parent material is lost by weathering by the time material reaches the top of the saprolite, as indicated by a chemical depletion fraction, CDF (Riebe et al., 2003), of 0.5 (Hewawasam et al., 2013). The minerals affected by weathering are successively pyroxene, biotite and plagioclase, as shown by a mineralogical investigation of the corestone (Hewawasam et al., 2013). Plagioclase is the first mineral dissolved to completion at the corestone-saprolite boundary as indicated by the full removal of Na and Ca at this depth, while biotite and pyroxene continue to weather further up in the saprolite profile.

In the present study, detailed textural, chemical, and mineralogical analyses were performed on a subset of samples from the whole weathering profile of Hewawasam et al. (2013) (Figure 1A and B). In addition, we characterized an extensive set of samples from the spheroidally weathered corestone of Hewawasam et al. (2013). The sample set is listed in Table 1, and includes samples from the corestone (zone 1 to zone 4, Figure 1B), from the lower saprolite (samples SL 25 to SL 21), from the transition zone between the lower and upper saprolite (sample SL 17), from the upper saprolite (samples SL 14 to SL 8), and from the soil layer (sample SL 6).

2.2 Methods

Detailed analyses were performed to identify the transformation pathways during the weathering reactions. Textural and porosity changes were determined by analyses of particle size distribution, BET-specific surface area measurements (SSA) and He-pycnometry. Crystalline and amorphous secondary phases were identified and quantified by selective extraction of (non)crystalline Al- and Fe-(oxy)(hydr)oxides with dithionite and NaOH, FTIR spectroscopy, X-ray powder diffraction, electron microprobe analyses (Appendix A: Electronic Annex), and Fe-redox analyses.

2.2.1 Textural characterization

2.2.1.1 Particle size determination

Samples, previously sieved to < 2 mm, were gently crushed using a hand mortar to break up large aggregates (saprolite and soil samples) and solid corestone samples (cylinders obtained by drilling).

After removal of Fe-(oxy)(hydr)oxides with dithionite (see section 2.2.3), the samples were separated into three particle size fractions (sand: 2000 µm – 63 µm, silt: 63 – 2 µm, and clay: < 2 µm) by gravitational settling in a water column of the clay-sized minerals and wet sieving of particles > 63 µm at the Institute of Soil Science, Universität Hannover, Germany. The amounts of silt- and sand-sized fractions were determined by direct weighing after drying, and the weight difference to the bulk sample weight was attributed to the clay-sized fraction. Hence, the size fractions for sand and silt are minimum values, while those for the clay-sized fractions are maximum values. Moreover, we acknowledge that the initial gentle crushing of solid corestone samples can slightly bias the particle size distribution towards finer grain sizes. However, from visual observations during crushing this effect is most likely small (< 5% relative) as compared to the overall estimated uncertainty of the method (< 15% relative), especially regarding the uncertainty in determination of the clay-sized fraction by difference (< 20% relative).

2.2.1.2 Specific surface area (SSA) – BET analyses

About 1 g of sample (loose saprolite, and cylindric drill cores from the corestone and the rindlets) was left to degas in a FlowVag Degasser from Quantachrome Instruments. After complete degassing, the specific surface area was measured with a NOVA 4000e surface area & pore size analyzer from Quantachrome Instruments using N_2 and the BET method (Brunauer et al., 1938) at the Institute of Soil Science, Universität Hannover. The uncertainty and the smallest detectable SSA are ±0.01% and 0.01 m^2/g (detection limit), respectively (Quantachrome Instruments). Because the sample volume is small, we emphasize that there is an important difference between the detection limit and the limit for properly quantifying SSA. As corestone samples are cylindric drill cores and not powders, for these samples the specific surface area rather describes a connected internal surface area of N_2 accessible grain boundaries, and micro-fractures.

2.2.1.3 Porosity – He-pycnometry measurements

He-pycnometry measurements were performed to quantify the connected porosity. Cylinder-shaped samples with a defined volume V_{sample} (diameter 1 cm, height 2.0 to 2.5 cm) were drilled from the corestone and its first rindlet (outer rindlets were too friable to obtain a sample with a precise volume), and polished afterwards to obtain an even surface. Prior to measurements, cylinders were dried and weighed. After weighing they were exposed to a pressure of 19 kbar in a AccuPyc 1330 He-pycnometer (Micromeritics) at GFZ Potsdam. The measurement of the volume of gas V_{pore} that is displaced provides a quantification of the connected porosity. The porosity ϕ [vol%] can be determined with the following equation (Palacio et al., 1999):

$$\phi = \left[1 - \left(\frac{V_{total} - V_{empty}}{V_{sample}}\right)\right] * 100 = \left[1 - \left(\frac{V_{pore}}{V_{sample}}\right)\right] * 100 \quad (1)$$

V_{empty} is the volume of displaced gas in the empty sample holder. V_{total} is the volume of displaced gas in the sample holder containing the sample. The repeatability (five repeats) of sample volumes is 0.02%, and the accuracy is within 0.03% of gas displacement reading plus 0.03% of the sample chamber volume. Relative uncertainty on the measured porosity results is estimated to be < 2.3%.

2.2.2 Clay mineralogy – FTIR and XRD

The primary minerals in the Hakgala rock and in regolith bulk material are reported in Hewawasam et al. (2013). In order to identify the crystalline weathering products, we separated the clay-sized fractions of the samples and analyzed them using X-ray powder diffraction (XRD) and Fourier transformed infrared (FTIR) spectroscopy at the Institute of Soil Science, Universität Hannover. For XRD measurements, binding sites for exchangeable cations of the clay fraction were saturated with Mg^{2+} (Moore and Reynolds, 1997). The aliquots for Mg^{2+} saturation were taken from the clay suspension after dithionite extraction (see section 2.2.3) and separation of the clay sized fraction (see section 2.2.1.1). The Mg^{2+} -saturated suspension was transferred to a glass slide and left to dry at room temperature to obtain oriented samples. As the clay-sized fraction of corestone zones 1 and 2 is dominated by fragments of primary minerals rather than by secondary weathering products, we do not report the XRD and IR patterns of these two samples. X-ray diffraction patterns were acquired using a Siemens D 500 diffractometer, with Cu-Kα radiation, with a resolution of about 0.01° 2 Theta. Peak maxima were identified using the PowDLL software (Kourkoumelis, 2013). Infrared spectroscopy measurements were performed on clay-sized fractions in transmission mode using KBr pellets (*e.g.*, Balan, 2006; van der Marel and Beutelspacher, 1976). About 1 mg of each dried clay separated fraction of the samples (treated previously with dithionite, see section 2.2.3) and 300 mg KBr were gently homogenized in a mortar and pressed to transparent pellets. Transmission spectra were recorded with a Bruker Tensor 27 FTIR spectrometer in a wavelength range from 400 to 4000 cm^{-1}, at a resolution better than 1 cm^{-1}, and a wavelength accuracy of 0.01 cm^{-1}. The spectra were evaluated using the OPUS software (Bruker).

2.2.3 Selective extraction of amorphous phases and oxides using dithionite and NaOH

Extractions of secondary oxides from the samples were performed using (a) sodium dithionite ($Na_2S_2O_4$) to release chemical elements from (non)crystalline Fe-(oxy)(hydr)oxides (mostly containing Fe, Al, Mn, and Si); and (b) NaOH to extract chemical elements from amorphous phases (mostly containing Al and Si). Corestone samples were gently crushed using a hand mortar prior to the treatment. Dithionite extractions were conducted on bulk samples following Mehra and Jackson (1960) and Schwertmann (1964). The two-step extraction procedure involved 3 h leaching at 72 °C in dithionite solution buffered with citrate bicarbonate, followed by another 30 min leaching after fresh dithionite addition. After sampling of an aliquot from the solution for chemical analyses of dissolved elements, the remaining suspension was used for grain size analysis, FTIR and XRD measurements of

the clay sized fraction (< 2 µm). Extractions with 0.5M NaOH were performed for 4 h in a boiling steam bath on bulk samples following Foster (1953) and Sauer et al. (2006). The chemical composition of the leachates was measured in 0.15M HNO_3 with a Varian ICP-OES at the Institute of Soil Science, Universität Hannover, with a relative analytical uncertainty of 5% (estimated from repeat measurements on reference materials).

2.2.4 Fe(II)/Fe_{total} ratios

Fe(II)/Fe_{total} ratios were measured following the method described in Schuessler et al. (2008) at the Institute of Mineralogy, Universität Hannover. About 15 to 20 mg (corestone) or 5 to 20 mg (saprolite and soil) powdered sample aliquots (depending on the expected Fe(II), Fe(III) and total Fe concentration) were digested in a HF-vanadate mixture using V(VI) as a carrier for Fe(II). The Fe(II) concentrations were measured with an UV/VIS spectrometer (UV-1800, Shimadzu). The amount of Fe_{total} was determined on the same analyte solution after Fe(III) reduction with hydroxylamine hydrochloride. The measurement sequence included a procedure blank (< 3% of processed Fe and therefore considered insignificant) and the USGS BIR-1 basalt and ANRT GS-N granite reference materials for data quality control. Uncertainty in Fe(II)/Fe_{total} ratios is ±0.03 (2SD), based on repeat measurements of certified reference materials (Schuessler et al., 2008).

3. Results

3.1 Textural characterization

The range of the clay-sized fraction (< 2 µm) is 2 – 4% in the corestone, and increases to 56% in the upper saprolite (Figure 2A, Table 1). It becomes the dominant size fraction at about 150 cm depth. However, the clay-sized fraction is slightly lower in the soil than in the upper saprolite. The silt-sized fraction ranges from 14.7 to 16.6% in the corestone. In the regolith, the silt-sized fraction ranges between 6.6 and 29.3% with lower values towards the top. The fraction of sand-sized minerals is 80.1 – 83.4% in the corestone. In the regolith its contribution decreases from 74.8% in the lower saprolite to 36.6% in the soil.

Porosity is below the detection limit of the He-pycnometry method in corestone zone 1 (pores are too small to be entered by He atoms). In corestone zone 2 the porosity is 0.89 ±0.02 vol.% and increases in corestone zone 3 to 1.66 ±0.04 vol.% and to 12.57 ±0.28 vol.% in corestone zone 4 (Figure 2B, Table 1, errors are absolute values, the relative error is < 2.3% of porosity). The connected internal surface area of grain boundaries and micro-fractures is below the detection limit of the BET method (< 0.01 m^2/g using N_2) in corestone zone 1, but zone 2 has a connected internal surface area of about 3 m^2/g, similar to zone 3. The connected internal surface area then increases towards the rindlets in zone 4 to 4.6 m^2/g. In the saprolite, specific surface area (SSA) increases from 15.1 m^2/g above the corestone to 55.6 m^2/g in the upper saprolite (Table 1).

3.2 Clay mineralogy

The clay mineral assemblages were identified from FTIR and XRD analyses by comparison to published reference data (Balan, 2006; Gustafsson et al., 1999; Hong et al., 2012; Moore and Reynolds, 1997; van der Marel and Beutelspacher, 1976) and results are compiled in Table 2 and Figure 3. Note that due to the dithionite treatment prior to the grain size separation Fe-(oxy)(hydr)oxides do not appear in FTIR spectra and XRD pattern. The FTIR spectra are shown only in the range of 3800 – 3300 cm^{-1} (Fig. 3A), where peaks, specific of clay minerals, are located. Because the clay-sized fraction in corestone zones 1 and 2 is dominated by primary minerals, the results for these corestone zones are not reported in Figure 3. Importantly, and in contrast to the extractions of the (non)crystalline (oxy)(hydr)oxides, the clay mineralogical analyses were only performed on the clay-sized fraction separates.

Characteristic peaks for clay minerals in the spectra are close to background level for corestone samples, but clearly detectable in saprolite and soil samples. Combining results from both analytical techniques (XRD and FTIR), kaolinite can be identified as the major secondary clay mineral throughout the regolith, followed by gibbsite. In some cases quartz and feldspars are detected in the clay-sized fraction. The broadening of the strong XRD kaolinite peak at 7.3 Å towards higher values (*e.g.*, SL 21, Figure 3B) can be explained by inter-stratification of halloysite or smectite layers, but for simplification we do not differentiate between "pure" kaolinite and mixed-layer kaolinite minerals, and in the following the term kaolinite is used interchangeably. Minor peaks in the region 10 – 20 Å can be attributed collectively to a group of 2:1 sheet silicates (biotite) and clay minerals: smectite, vermiculite, illite, and chlorite. Distinguishing between these minerals and potentially mixed-layer minerals is more challenging. However, we first note that in most samples (except in upper saprolite and soil) these peaks are relatively small, suggesting that their contribution to the mineral assemblage is almost negligible. Second, although mixed-layer clay minerals with a high biotite component can produce the XRD peaks observed around 10 Å (Figure 3B), the XRD peak at 12 Å might rather reflect a regularly interstratified phase containing alternating 14 Å and 10 Å layers, *i.e.*, 2:1 clay layers within the biotite minerals (mixed layer clays), or poorly hydrated smectites. Expansion of the biotite layers, due to hydration (hydrobiotite), oxidation, or replacement of K by other cations could also shift the 10 Å biotite peak to higher values (Kalinowski and Schweda, 1996; Malmström and Banwart, 1997). The presence of 2:1 clay minerals can also result in XRD peaks such as those observed at 14 Å and the broad XRD peaks between 18 and 20 Å. No further analyses were carried out to distinguish between the different secondary 2:1 clay minerals, as the peak intensities are too low for an identification of the individual minerals. Nevertheless, as Na and Ca are almost entirely solubilized from the whole regolith at Hakgala (Hewawasam et al., 2013) montmorillionite- or nontronite-like smectites are unlikely to be present, as well as illite and chlorite as this highly weathered profile has developed under tropical climate (Hong et al., 2009; Robert and Kennett, 1994). Hence, we infer that these 2:1

clay minerals are most likely smectite and vermiculite. In addition, we point out that these minerals are most likely of Fe-rich chemical composition, as Fe is supplied through pyroxene and biotite weathering (see below) and is not removed from the system (Hewawasam et al., 2013).

3.3 Selectively extracted (non)crystalline (oxy)(hydr)oxides

The dithionite-soluble Fe (Fe_d) ranges from 0.01 to 4.1 wt.% over the entire profile. Normalizing the concentration of Fe_d to total Fe concentration from bulk XRF analyses (Hewawasam et al., 2013) yields the fraction of Fe that is carried by (non)crystalline Fe-(oxy)(hydr)oxides. The Fe_d/Fe_{total} ratio is 1.5% in corestone zone 1, 0.6% in zone 2, 11.2% in zone 3, 11.8% in zone 4a and 9.2% in zone 4c (Figure 4A, Table 1). In the saprolite the Fe_d/Fe_{total} ratio increases to 32.0%, from the corestone to the transition zone in the saprolite at 435 cm depth, and increases again to 47.9% in the upper saprolite. The soil exhibits a Fe_d / Fe_{total} ratio of 37.8%. The dithionite-soluble Mn (Mn_d) in the corestone was too low for quantitative determination by ICP-OES in the extracts (*i.e.,* indistinguishable from blank level concentrations). In the saprolite, the Mn_d/Mn_{total} ratio is relatively consistent in the lower and the upper saprolite with values between 57.4% and 87.4%. However, towards the soil Mn_d/Mn_{total} decreases to 36.2%. The soil exhibits a Mn_d/Mn_{total} ratio of 25.7% (Figure 4B). The concentration of Al contained in dithionite-soluble phases (Al_d) ranges from 0.01 wt.% to 1.0 wt.%, corresponding to a dithionite-soluble Al fraction (Al_d/Al_{total}) of 0.1% in zone 1 to 1.5% in zone 4c. In the saprolite profile, the Al_d/Al_{total} ratio increases from about 1% in the lower saprolite to 8.6% in the soil (Figure 4C). Only a small amount of Si is extracted by dithionite (Si_d), ranging from 0.02 to 0.1 wt.%, and Si_d/Si_{total} is < 0.3% throughout the profile (Figure 4D).

Aluminum and silicon contained in NaOH-soluble phases (Al_{NaOH} and Si_{NaOH}) show the same trend in the corestone but differ in the upper saprolite. The Al_{NaOH} increases from 0.04 wt.% in the corestone to 2.3 wt.% in the saprolite; Al_{NaOH} / Al_{total} in the corestone is between 0.5% and 14.2% (Figure 4E, Table 1). In the saprolite and the soil the fraction Al_{NaOH}/Al_{total} ranges from 10.6% to 20.1% with no clear trend. The measured Si_{NaOH} concentrations range between 0.2 and 1.3 wt.%. This corresponds to Si_{NaOH}/Si_{total} ratios of 0.5% to 3.2% in the corestone and 2.3% to 5.1% in the saprolite and soil (Figure 4F).

The contribution of (non)crystalline Al- and Fe(oxy)(hydr)oxides (Σ_{d+NaOH}, in oxide %wt., Table 1) to the bulk sample mass was calculated assuming that the amorphous phases are fully oxidized (*i.e.*, Fe is present as Fe(III) and Mn as Mn(IV)). Σ_{d+NaOH} ranges from 0.6% in corestone zone 1 to 5.3% in corestone zone 4, and increases to 6.5% in the lower saprolite. In the upper saprolite, Σ_{d+NaOH} is in the range of 6.6% and 13.6% and decreases to 9.7% in the soil.

3.4 $Fe(II)/Fe_{total}$

The corestone samples from zone 1 (samples 1.1 to 1.3) and the samples from zone 2 (light grey part in the corestone, samples 2.1 to 2.3) show no significant change in the $Fe(II)/Fe_{total}$ ratio (93 – 94%, Figure 4G, Table 1). Changes occur at the boundary from zone 2 to zone 3. This transition is macroscopically distinct as a darker band between the light gray zone 2 and the yellow zone 3 (Figure 1B). Values in zone 3 show no trend and are in the range 78 – 79%. The two rindlets around the corestone are slightly more oxidized, with ratios of 68% and 70% for samples 4a and 4c, respectively. The lower saprolite samples depict a strong decrease in Fe(II) content, with a $Fe(II)/Fe_{total}$ ratio changing from 44% above the corestone to 1% at a depth of about 300 cm. The $Fe(II)/Fe_{total}$ ratio increases again in the upper saprolite towards the top from 3% to 44% in the soil sample.

4. Discussion

4.1 The sequence of weathering reactions

In the following, we interpret the results to derive the sequence of reactions leading to the conversion of bedrock into saprolite and soil. In this respect, the spatial sequence of samples, investigated from the center of the corestone towards the rindlets and saprolite, directly corresponds to the progress of weathering with time.

4.1.1 Corestone zone 1: virtually unweathered bedrock

Besides fracturing into and around pyroxenes, electron microscope observations suggest that all minerals in zone 1 are unweathered (Hewawasam et al., 2013). Detailed textural characterization neither reveals any measurable connected porosity nor connected internal surface area of grain boundaries and micro-fractures, as their values are below the detection limit. For these reasons, corestone zone 1 can be considered as the starting material of the whole weathering sequence. Accordingly, only a small contribution of amorphous secondary phases was detected (< 0.6 wt.% of total mass, as calculated from the sum of dithionite- and NaOH-soluble major elements) showing only minor alteration of bedrock in zone 1 (Figure 4, Table 1).

4.1.2 Corestone zone 2: onset of weathering processes with pyroxene weathering

Corestone zone 2 shows strong evidence for weathering: (a) connected internal surface area of grain boundaries and micro-fractures measured by the BET method and porosity become detectable (Figure 2); (b) dithionite- and NaOH-soluble secondary phases are present (Table 1, Figure 4); and (c) microscopic observations reveal weathering of pyroxene (*e.g.*, Fe-oxide coatings along cracks in the pyroxene), while plagioclase remains unaltered (Hewawasam et al., 2013). The selective extraction experiments show that Fe-(oxy)(hydr)oxides form (Figure 4a), most likely as a result of pyroxene weathering. Weathering of pyroxene to goethite was also reported by Colin et al. (1990), Delvigne (1983), Merino et al. (1993), and Noack et al. (1993).

4.1.3 Corestone zone 3: sharp plagioclase weathering front and significant increase in porosity

Compared to the innermost layers, corestone zone 3 exhibits higher porosity (Figure 2), presence of kaolinite and 2:1 sheet silicates (Figure 3), higher concentration of dithionite- and NaOH-soluble phases, and larger extent of Fe oxidation (Figure 4). In addition to pyroxene, biotite and plagioclase also show weathering features in this zone (expansion of the layers in biotite and dissolution along grain boundaries and cracks in plagioclase; Hewawasam et al., 2013). Biotite weathering therefore also contributes to the decreasing $Fe(II)/Fe_{total}$ and to the Fe-(oxy)(hydr)oxides observed there.

4.1.4 Corestone zone 4: Rindlet formation

Zone 4 is characterized by a high porosity and slightly higher connected internal surface area values than in zone 3. Here, secondary crystalline products (2:1 clay minerals and gibbsite) are still close to the detection limit of XRD and FTIR (Figure 3), whereas large fractions of element contents (*e.g.*, Fe, Al, Si) are hosted by amorphous phases (Figure 4). Note that the clay mineral analyses were carried out on the clay-sized fraction separates only, which make up 4% of the bulk sample (Table 1), whereas the non-crystalline phases were extracted from bulk samples. Therefore, we can infer that in this zone weathering products are still mainly of amorphous character. The incipient gibbsite precipitation most likely results from crystallization of the Al-amorphous precursor produced after plagioclase dissolution (Balan, 2006; Dahlgren et al., 1997; Merino et al., 1993). Additionally, the decreasing amount of Fe(II), inferred from the $Fe(II)/Fe_{total}$ ratio of 68 – 70% is an indicator for ongoing weathering of pyroxene and biotite (Figure 4).

4.1.5 The rindlet-saprolite boundary

Saprolite is formed at the rindlet-to-saprolite boundary. At this boundary the content of clay-sized minerals and the specific surface area (SSA) increase sharply (Figure 2). While the rindlets exhibit a $Fe(II)/Fe_{total}$ ratio of 68%, the lower saprolite shows a significantly higher degree of oxidation of the Fe-bearing primary minerals ($Fe(II)/Fe_{total}$ < 44%, Figure 4). Presumably this oxidation can be attributed to biotite and minor amounts of pyroxene still remaining unweathered at the rindlet-saprolite boundary. As shown by electron microprobe analyses (Appendix A,: Electronic Annex), Mn is mostly hosted in pyroxenes and thus can be used as a proxy for pyroxene content. Furthermore, no secondary crystalline Mn-bearing phases could be detected by XRD or FTIR in the corestone and the rindlets. Therefore, Mn is soluble in the corestone and the rindlets (although it is incorporated into secondary phases in the regolith, as revealed by the Mn_d/Mn_{total} ratio). As a loss of 75% Mn is shown by the mass transfer coefficient τ of Mn (τ_{Mn}) in the outermost rindlet (Hewawasam et al., 2013), we can infer that at least 75% of the pyroxene is dissolved before the solid material enters the saprolite *per se*. However, small amounts of Mn-bearing secondary precipitates might remain undetected, thus leading to an underastimation of this pyroxene loss.

4.1.6 The saprolite and the formation of kaolinite

Throughout the lower saprolite the parameters showing the most striking changes are particle size distribution, SSA (Figure 2), and the $Fe(II)/Fe_{total}$ ratio decreasing to near zero at approximately 3 m depth in the upper saprolite (Figure 4). Therefore, all Fe-bearing primary minerals are weathered to completion at this depth. As the amount of gibbsite decreases upward in the profile and as 2:1 clay minerals were not found in the saprolite, kaolinite appears to be the final weathering product. The formation of kaolinite is confirmed by the amounts of clay-sized particles that strongly increase towards the top of the profile and from the XRD and FTIR patterns. The formation of kaolinite in the saprolite requires a source for Si, which could be the weathering of K-feldspar and the decomposition of the secondary 2:1 clays. Furthermore, the continuous increase of the contribution of dithionite-soluble phases reveals increasing amounts of Fe-(oxy)(hydr)oxides towards the top.

4.1.7 The formation of soil from saprolite

In contrast to the saprolite, where kaolinite and Fe-(oxy)(hydr)oxides are the major secondary minerals, secondary 2:1 clay minerals are abundant in the soil. Like gibbsite, the abundance of secondary 2:1 clay minerals and the $Fe(II)/Fe_{total}$ ratio are increasing towards the top. We contend that mineralogical and chemical transformations within the soil layer are disconnected from those in the saprolite beneath it. Chemical reactions within the soil system can be influenced and altered by redox processes, pH changes, clay translocation, biological activity and external inputs, for example. In particular, dust can add primary and secondary minerals to the system and dust dissolution can in turn impact the pore-water chemistry. Evidence for dust input to the Hakgala soil was found using mass transfer coefficients and radiogenic Sr isotope analyses (Hewawasam et al., 2013).

4.2 Fracture versus porosity formation across the corestone and the rindlets

Within the regolith column, fluids can circulate relatively easily because of the fragmented fabric and the high porosity, as indicated by the large SSA values (Figure 2). Throughout the corestone, microscopic observations together with connected internal surface area and porosity measurements suggest that an initial network of fluid pathways has developed in the form of connected pores and fractures, similar to the pathways described in Buss et al. (2008), Fletcher et al. (2006), or Navarre-Sitchler et al. (2013). However, these pathways are absent in corestone zone 1, *i.e.,* during incipient weathering, where porosity was below the detection limit. Therefore, reactive phases (*e.g.*, O_2, protons) can reach minerals only through (i) fractures of a scale larger than our observational scale of a few cm, followed by (ii) migration along grain boundaries. In corestone zone 2 and further outwards, porosity and connected internal surface area of grain boundaries and micro-fractures reach measurable values (Figure 2), suggesting that reactive phases (including fluids) can percolate through connected pore spaces or a network of fractures. In particular, the formation of rindlets separated from each other

by macroscopic fractures suggests that specific volume changes induced by mineral reactions build up sufficient strain to produce fracturing.

In the following section we discuss how such secondary porosity by fractures and open pore space might form in each zone of the corestone to promote mobility of reactive phases. In this regard it is important to note that formation of fractures requires the build-up of strain during reactions with a positive volume change, while open pore space is formed during reactions with a negative volume change. It should also be noted that both processes (fracture formation following a positive volume change and formation of open pore space during a negative volume change) ultimately produce porosity.

4.2.1. Strain formation by *in situ* Fe oxidation in pyroxene and biotite

In situ Fe oxidation (meaning oxidation of structural Fe(II) within the mineral lattice without inducing mineralogical phase transformations, *e.g.*, see Buss et al., 2008) in pyroxene and biotite is the first weathering mechanism occurring in the corestone, implying that O_2 is the reactive phase driving the onset of weathering. As this process produces strain, following Fletcher et al. (2006) we hypothesize that this Fe(II) oxidation eventually leads to the formation of macro-fractures separating the rindlets from the corestone during spheroidal weathering. Because the porosity is low in the corestone center and fractures are not observed at the scale of our sample we assume that oxygen is transported along grain boundaries. Hence, below we consider the transport of O_2 in the gaseous form. To test our hypothesis, we calculate the relative volume increase, and elastic strain ε, due to the iron oxidation reaction:

$$FeO + \frac{3}{2}H_2O + \frac{1}{4}O_2 = Fe(OH)_3 \quad (2)$$

Fracturing will occur if the elastic strain ε caused by *in situ* oxidation during chemical weathering overcomes the fracture surface energy Γ, following the fracture criterion:

$$2\Gamma = \frac{E\varepsilon^2}{1-\nu} = U \quad (3)$$

Where E is Young's Modulus, ν is Poisson's ratio (values are listed in Table 3) and U is the strain energy density that must overcome 2Γ in order to fracture the rock. This fracture criterion can be tested for each layer of the corestone, using elastic strain values calculated as:

$$\varepsilon = \frac{1}{3} * \frac{\Delta V_{rock}/M_{rock}}{V_{rock}/M_{rock}} = \frac{1}{3} * \Delta\tilde{V} * \rho_{rock} \quad (4)$$

Where M_{rock}, V_{rock}, and ρ_{rock} are the mass, volume, and density of rock being subjected to weathering, respectively [kg_{rock}, m^3, and kg_{rock}/m^3, respectively]. ΔV_{rock} is the volume change of this rock mass

during oxidation of pyroxene and biotite [m³]. $\Delta\tilde{V}$ is the corresponding volume change relative to mass rock unit [m^3/kg_{rock}], which can be calculated as:

$$\Delta\tilde{V} = \frac{\Delta V_{rock}}{M_{rock}} = V_{FeO} * \left([Fe]_{bt,0} * \left(1 + \tau_{bt,j}\right) - [Fe]_{bt,0}\right) + V_{FeO} * \left([Fe]_{px,0} * \left(1 + \tau_{px,j}\right) - [Fe]_{px,0}\right) + V_{Fe(OH)_3} * \left([Fe(OH)_3]_j - [Fe(OH)_3]_0\right) \quad (5)$$

$V_{Fe(OH)3}$ and V_{FeO} [m³/kg] are the specific volumes of $Fe(OH)_3$ and FeO, respectively (Robie and Hemingway (1995), Tables 3 and 4). $[Fe]_{(bt,px),0}$ [in kg/kg_{rock}] represents the concentration of biotite (bt)- and pyroxene (px)-borne Fe in the rock, respectively (Appendix A: Electronic Annex). $\tau_{(bt,px),j}$ (Table 5) is the mass transfer coefficient (Brimhall and Dietrich, 1987) of biotite and pyroxene in weathered layers j, respectively (*i.e.*, minus the fraction of initial biotite and pyroxene weathered). $[Fe(OH)_3]_j$ is the $Fe(OH)_3$ concentration in the weathered layer j. $[Fe(OH)_3]_0$, the initial $Fe(OH)_3$ concentration in the rock, is set to be zero. In the corestone center only 5% of total Fe is ferric and is most likely of primary bedrock origin. Hence, it does not result from oxidation reactions and therefore can be neglected for this purpose. The values of these parameters are listed in Tables 3 and 4. Precipitation of clay minerals, another mechanism entailing a volume increase, was hypothesized by Jamtveit et al. (2011), Jamtveit et al. (2008), Røyne et al. (2008), and Rudge et al. (2010) to produce hierarchical fractures. However, in our corestone clay mineral precipitation is first initiated in zone 3 and even there the amount of clay minerals formed is not of significance. Therefore, we do not quantify the strain build-up during formation of clay minerals, which is unlikely to affect the volume budget near the weathering front.

To fulfill Eq. (3), we calculate that 7.71 x 10^{-3} kg/kg_{rock} (7.22 x 10^{-2} mol/kg_{rock}) FeO needs to be oxidized, corresponding to approximately τ_{px} = -0.25 or τ_{bt} = -0.34 (25% pyroxene or 34% biotite oxidation). The boundary at which this criterion is attained is the first point at which the strain increase overcomes the resistance of the rock to fracture. A worked example of this calculation is provided in Appendix A: Electronic Annex. The outermost position at which such degree of oxidation (combining biotite and pyroxene oxidation) is reached, is between zone 2 and zone 3 (Table 6). However, in contrast to this prediction the innermost macroscopic fracture (fractures separating the rindlets from the corestone) is detected more outwards, at the boundary between zone 3 and zone 4. We note that the predicted position of fracturing is a conservative estimate, *i.e.*, based on the lowest biotite weathering intensity proposed by Hewawasam et al. (2013) and the smaller value for the biotite-specific molar volume (phlogopite, Table 4; Robie and Hemingway, 1995). Using a higher biotite weathering rate for a biotite molar volume of annite would result in a predicted position of fracturing that is even more inward. We also note that τ_{px} and τ_{bt} (tracked by the loss of Mn and Sr, respectively; Hewawasam et al., 2013) could be underestimated: as the *in situ* oxidation occurs before the dissolution of mineral crystal lattice, oxidation of pyroxene and biotite is most likely faster than the release of Mn and Sr.

However, a more accurate prediction of the position of the first fracture would also be closer to the core, hence even further from the observed position of fracturing.

We can attribute the apparent discrepancy between the predicted and observed positions of fracturing to two factors that are not mutually exclusive:

(1) The increasing strain due to Fe(II) oxidation is compensated by the production of additional open pore space during plagioclase dissolution and replacement by clay minerals with lower specific molar volume such as kaolinite in corestone zone 3. However, we note that in zone 2, plagioclase remains virtually unweathered. In zone 3 the strong increase in porosity (Figure 2), and thus compensation of elastic strain, can be attributed to plagioclase weathering.

(2) Micro- rather than macro-fractures (as hypothesized by Fletcher et al., 2006) are formed following strain build-up. In this case, the micro-fractures that we infer from the measurable porosity in zone 2 form in the direct vicinity of the oxidized minerals, where they accommodate the strain generated by Fe(II) oxidation. Only when a certain size and density of these micro-fractures is reached do they merge to form the macroscopic fractures separating the rindlets (Navarre-Sitchler et al., 2013). At Hakgala, we suggest that the macroscopic fractures form only in zones 3 and 4. The increase in porosity and connected internal surface area of grain boundaries and micro-fractures in corestone zone 2 supports the micro-fracture formation hypothesis. Bazilevskaya et al. (2015) also report that oxidation of biotite is the first weathering process causing micro-fracture formation, with these micro-fractures allowing then for fluid infiltration and hence dissolution of plagioclase. This finding is consistent with our observations for the Hakgala site, where the dissolution front of plagioclase (consumption of protons, zone 3) lies higher than the O_2 consumption front (zone 2).

In this regard, we note that our observations differ from the multi-mineral model of Lebedeva et al. (2007), which predicts (a) a zone of reduced porosity immediately surrounding unweathered rock that is caused by oxidation of Fe-bearing primary minerals and (b) an outer zone with higher porosity following plagioclase dissolution. In contrast, in the Hakgala corestone the Fe(II) oxidation zone is characterized by an increase in porosity (actually due to fracturing following Fe(II) oxidation). We note that this discrepancy might be ultimately due to the fact that the bedrock in the study of Lebedeva et al. (2007) already exhibits some connected porosity, while the bedrock in Sri Lanka does not. Although Lebedeva et al. (2007) acknowledge that this low-porosity layer could be a locus of fracturing in any case, their model does not take into account the fluid pathway provided by fractures. Our findings indicate that such pathways are important and that in multi-mineral weathering systems the importance of strain *versus* secondary porosity budget has to be taken into account.

4.2.2 Weathering pathways and associated volume changes

We have shown that the competition between volume increase and formation of secondary porosity generates fluid pathways. Therefore, we combine the results from porosity measurements and analyses of the secondary phases to reconstruct mineral-specific weathering pathways (for pyroxene, biotite, and plagioclase) in the corestone, where the initiation of weathering occurs. These are depicted schematically in Figure 5 and listed in Table 7. An important constraint in this reconstruction is the fact that amorphous phases are present deeper in the corestone (*i.e.*, appear earlier in time) than secondary clay minerals. This is shown in particular by the observation that amorphous phases were detected in bulk samples in the corestone, whereas clay minerals were barely detectable even in the separated clay-sized fraction. This can be interpreted in two ways. First, the solid products of weathering reactions might differ depending on where they occur in the regolith profile (*e.g.*, corestone *vs.* saprolite), as permeability, porosity, and chemical composition of reactive phases (including fluids) vary with depth within the regolith. Second, many weathering reactions have been shown to involve an amorphous precursor (Chadwick and Chorover, 2001; Dahlgren et al., 1997; Hellmann et al., 2012; Steefel and van Cappellen, 1990), which is our preferred interpretation here. Therefore, for a given primary mineral, we suggest that a distinction should be made between the "primary mineral dissolution front" and the “secondary clay crystallization front” (Figure 5, the only exception at Hakgala might be weathering of biotite to kaolinite by direct transformation or dissolution and re-precipitation; Dong et al., 1998; Murphy et al., 1998).

Pyroxene weathering starts in zone 2 (Hewawasam et al., 2013) with *in situ* oxidation and leads to the formation of an Fe-bearing amorphous precursor and Fe-(oxy)(hydr)oxides (goethite was identified with XRD) as revealed by the dithionite extraction, and most likely in zone 3 an Fe-rich smectite-like intermediate clay mineral eventually transformed to crystalline Fe-(oxy)(hydr)oxides and kaolinite in the saprolite (Figure 5). Biotite weathering (after oxidation) produces an Fe- and Al-bearing amorphous precursor along with Fe-(oxy)(hydr)oxides, kaolinite or 2:1 mixed layer biotite (hydration of biotite and formation of mixed layer biotite-vermiculite, or biotite-smectite), eventually leading to the formation of Fe-(oxy)(hydr)oxides and kaolinite (Figure 5). We acknowledge that we do not distinguish between abiotic or biotic induced weathering reactions (Bonneville et al., 2009; Shelobolina et al., 2012). In addition, although processes at the mineral scale (nm) are not discussed here, we note that oxidation of biotite might be accompanied by K-loss from the interlayer and expansion of the layers (Bonneville et al., 2009; Bray et al., 2014; Buss et al., 2008; Kalinowski and Schweda, 1996; Malmström and Banwart, 1997). Plagioclase weathering is also initiated in zone 3 and most likely contributes to the formation of the Al-amorphous precursor, as kaolinite was barely detected. This amorphous precursor is converted into crystalline gibbsite and kaolinite in the rindlets where plagioclase weathering is intense (Figure 5).

4.2.3 Spatial sequence of strain and porosity formation

Due to gaseous O_2 transport along grain boundaries and subsequent *in situ* Fe oxidation in pyroxenes in zone 2 the sequence starts with the build-up of strain in and around the oxidizing mineral. As stated previously, and importantly, such *in situ* Fe oxidation does not entail mineralogical phase transformations (see section 4.2.1). Rather, this strain increase induces micro-fractures in the minerals within the vicinity of the oxidized minerals, as already reported by Bazilevskaya et al. (2015). The micro-fractures are measurable as porosity increases in this zone, and serve as pathways for reactive phases (e.g., O_2, protons) and promote the weathering of the primary minerals. The first mineral transformation observed in zone 2 is the conversion of pyroxene to Fe-(oxy)(hydr)oxides that also contributes to porosity increase because this reaction involves a negative volume budget and hence formation of pore spaces. The onset of biotite weathering could not be unequivocally detected, but starts with *in situ* Fe oxidation between zones 2 and 3, adding to the strain and triggering further micro-fracture formation. The porosity increase is then sufficient enough to allow for efficient transport of reactive phases (including aqueous fluids) leading to plagioclase dissolution in zone 3. In this zone formation of pore spaces increases dramatically and compensates for the strain caused by Fe oxidation. Therefore, the macro-fractures that separate the rindlets occur later than expected and separate zone 4 from zone 3. At this point, the micro-fractures and the pore spaces merge together to form the macro-fractures and production of rindlets. Within the rindlets, the weathering of plagioclase to kaolinite increases dramatically, producing many pore spaces. Therefore, the combination of fracture formation due to *in situ* Fe oxidation and the formation of pore spaces during weathering reactions that exhibit a negative volume budget leads to the conversion of bedrock to saprolite via spheroidal weathering.

Most of the reactions reveal an amorphous precursor (including Fe-(oxy)(hydr)oxides) that forms deeper in space, hence earlier in time, than secondary minerals (Figure 5). This observation is relevant for models showing that the fluid flow rate and the net precipitation rate of secondary minerals exert a substantial control over reaction rates, mass depletion and weathering advance rate (Maher et al., 2009). For example, it is expected that both the rate constants and the equilibria between fluids and secondary solids differ between amorphous and crystalline precipitates.

4.3 The role of O_2 transport in the feedback between erosion and weathering

We have shown that oxidation of Fe-bearing minerals is the limiting factor for the onset of the chemical weathering reactions at Hakgala and provides a possible feedback mechanism between erosion at the top of the profile and weathering at the bottom of the profile (Fletcher et al., 2006). This process requires the transport of O_2 from the surface where it is supplied in virtually unlimited amounts through the regolith to the weathering front, hence O_2 is the rate-limiting phase. We can now discuss how the relative importance of the type of O_2 transport (*i.e.*, diffusion *vs.* advection) through the Hakgala weathering profile influences the strength of this feedback. In a weathering system, where oxidative weathering is the process limiting the rate of regolith production, the strength of such a

feedback can be envisaged by a simple scenario in which an erosion event removes an infinitely small layer of topsoil, that we call *dz* (Figure 6A). As a result, regolith thickness decreases, and the weathering front comes closer to the surface, and hence to the atmosphere, by a distance equal to *dz*. As O_2 is consumed at depth and is supplied at the top, its concentration increases upward, and this lower distance between the weathering front and the surface results transiently in higher O_2 concentration (here called c_{wf}) at the weathering front. As a result, oxidative weathering will be enhanced and the weathering front will propagate further away from the surface, thereby increasing regolith thickness. The strength of this feedback mechanism is therefore dependent on the gradient of O_2 concentration, *dc/dz*, in the lowest part of the regolith, as suggested by Fletcher et al. (2006).

To explore these dependencies we developed a model in which transport of O_2 through a steady-state weathering profile occurs through both diffusion and advection. Advection can occur in regolith through macro-pores and fractures, while diffusion is more typical of transport through micro-pore networks prevailing near the weathering front or through clay layers in the regolith (Brady and Weil, 2007; Bazilevskaya et al., 2015). In our model, the boundary conditions are constant, meaning that erosion and regolith production are constant and balance each other, such that regolith thickness remains constant (such steady state condition applies to Hakgala, as shown by Hewawasam et al., 2013), and that the bedrock is homogenous with uniform amounts of Fe(II)-bearing primary minerals. For the sake of simplicity, and although O_2 is obviously consumed in the saprolite (as shown by $Fe(II)/Fe_{total}$ profiles, Figure 4), we assume that all O_2 is only consumed in a zone confined to the weathering front. Given these assumptions, the steady-state partial derivative equation for non-reactive transport of O_2 is:

$$\phi \frac{\partial c}{\partial t} = -v \frac{\partial c}{\partial z} + \phi D \frac{\partial^2 c}{\partial z^2} = 0 \quad (7)$$

Where ν is the advective velocity [m/s], D is the diffusion coefficient [m²/s], ϕ is the porosity, c is the concentration [mol/kg], z the depth [m], and t is time [s]. The first boundary condition is given by the atmospheric O_2 concentration, c_0, at the surface (z = 0) and the secondary boundary condition is given by the gradient of O_2, f [mol_{O2}/m^3*m] over a distance of about 3 m (defined by the corestone zone), which is located at about 8.3 m depth in the Hakgala weathering profile at the saprolite-corestone transition. For calculation purposes, we use non-dimensional variables:

$$C = c/c_0 \quad (8)$$

$$F = f * H/c_0 \quad (9)$$

$$Z = z/H \quad (10)$$

with c_0 the atmospheric O_2 concentration, and H the depth of the weathering profile. F is the non-dimensional flux of O_2 consumption at the lower boundary. The calculation of F for the Hakgala weathering profile is shown further down. The steady-state solution of equation 7 and of the associated boundary and initial conditions is:

$$C = 1 + \frac{F}{Pe} * [exp^{-Pe} - exp^{-Pe(1-Z)}] \quad (11)$$

The Péclet number, *Pe*, expresses the competition between advection and diffusion and is defined as:

$$Pe = \frac{advective\ transport}{diffusive\ transport} = \frac{-vH}{\phi D} \quad (12)$$

with v for velocity, H as a length scale, ϕ the porosity, and D the diffusion coefficient. Higher *Pe* numbers describe advection-dominated systems, whereas lower *Pe* numbers represent diffusion-dominated transport. In a natural system it is unlikely that only one *Pe* number characterizes the entire profile. However, for the purpose of this simple model, we neglect these variations and use a "profile-averaged" *Pe* number. In soils, the transport conditions can vary over a wide range in small spatial distances. Previous studies show that *Pe* numbers cover a wide range of values across different soils (*e.g.*, 5 to 69; Mayes et al., 2003). The relatively high *Pe* values indicate the importance of advection, although diffusion has been assumed to be the main mode of transport in weathering models (Brantley and Lebedeva, 2011; Lebedeva et al., 2010; Navarre-Sitchler et al., 2013). Bazilevskaya et al. (2015) found that in a supply-limited weathering regime, a combined transport of advection and diffusion will lead to thick weathering profiles, whereas transport only by diffusion will lead to thin weathering profiles. These authors also suggest that the oxidation-induced fracturing provides the condition for the combined diffusion-advection transport. We do not have any constraint on the *Pe* number of the Hakgala weathering profile, but as this is the only free parameter (F is constrained by our data, see below), we can perform a sensitivity analysis of the model output as a function of the *Pe* value.

The O_2 gradient f resulting from O_2 consumption at depth due to Fe oxidation can be determined by calculating the mass transfer coefficient τ of Fe(II) normalized to Zr (which was shown to be immobile by Hewawasam et al., 2013):

$$\tau_{Fe(II)} = \frac{[Fe(II)]_{weathered}}{[Fe(II)]_{parent}} * \frac{[Zr]_{parent}}{[Zr]_{weathered}} - 1 \quad (13)$$

We calculate the gradient for the entire approximately 3 m-thick corestone zone between the bedrock and the saprolite (over which corestones occur in the weathering profile). We assume that O_2 consumption in this entire zone occurs over an infinitely small layer at the lower boundary of the Hakgala weathering profile, comparable to the corestone zone. We use the change in Fe concentration and in $Fe(II)/Fe_{total}$ ratio from the corestone center to the outermost rindlet to calculate τ_{Fe}. With equation 13 we derive 28% oxidation of Fe(II) to Fe(III) (in total 6.62 x 10^{-3} kg_{Fe}/kg_{rock}, calculated with the average Fe concentration in the rock). If every mol Fe(II) consumes 0.25 mol O_2 (equation 2), the amount of O_2 per kg rock consumed during oxidation is about 2.95 x 10^{-2} mol_{O2}/kg_{rock}. The gradient of O_2 is f = 2.63 x 10^{-2} [mol_{O2}/m^3*m] at the saprolite-corestone transition in the Hakgala weathering profile. For this 3 m-thick corestone zone with an inferred porosity of 10% we calculate a non-dimensional gradient F = 2.42 x 10^{-1}. With this lower boundary condition, we can model the O_2

profile in the Hakgala regolith profile for different *Pe* numbers (Figure 6A, Table 8). Diffusion-dominated transport of O_2 results in a steeper O_2 gradient in the lowest part of the saprolite than in the case of transport dominated by advection. Therefore, following the scenario developed above, diffusive O_2 transport will lead to stronger feedbacks between erosion at the top and weathering at depth. Diffusion-dominated transport likely also leads to low weathering front advance rates (Brantley and Lebedeva, 2011) and would be comparable to the model of Fletcher et al. (2006). However, as shown by Lebedeva et al. (2010), natural systems with thick weathering profiles are typically characterized by combined diffusive-advective transport. In such systems a feedback will be weakened, for example, if there is a thick, purely advective layer at the top where atmospheric concentrations prevail throughout the depth profile, or if consumption of O_2 is not the rate limiting factor, and excess of O_2 prevails at the weathering front (*e.g.*, when Fe(II)-bearing minerals are absent). Then, both boundaries might act independently and the weathering profile can thicken or thin as no feedback is in operation.

Similar conditions as described in Navarre-Sitchler et al. (2013) may exist in our profile, where dominating advective transport (higher *Pe* numbers) is proposed to occur in the upper saprolite, along preferential pathways (like pore networks, pre-existing joints and cracks), and diffusion (lower *Pe* numbers) dominates the transport in the rock, the center of the separated rindlets and the lower saprolite. Because we used "profile-averaged" *Pe* numbers, lower *Pe* numbers may be most appropriate for the investigated profile to produce such a thick regolith as further discussed in the following section 4.4.

4.4 Tectonic and lithologic controls on the weathering rate

The setting in Sri Lanka is representative of a supply-limited weathering end member, where the mineral dissolution kinetics are faster than the supply of fresh material into the weathering reactor. Here, a thick saprolite profile prevails, where plagioclase is completely dissolved in the lower part, as also reported by Navarre-Sitchler et al. (2013). However, unlike the weathering profile (featuring corestones) discussed in Navarre-Sitchler et al. (2013), the Sri Lankan weathering rate is at the lower end of global weathering rates (5 – 60 t km^{-2} y^{-1}, Dixon and von Blanckenburg, 2012) despite the occurrence of Fe-bearing minerals. We first explore whether these rates provide an incomplete quantification of the total weathering flux. In this regard, it is important to note that these rates are based on *in situ* cosmogenic nuclides measured in quartz sampled in top soil. As these rates detect denudation from the surface layer they were corrected for solute loss at greater depth (Hewawasam et al, 2013). That these local rates are representative for the landscape scale was demonstrated by the similar rates derived from solute concentrations in streams (Hewawasam et al, 2013). Hence, we regard the processes derived from the detailed investigation of the weathering profile in this paper as those that govern weathering in the entire landscape. We next discuss possible reasons for these low weathering rates.

First, as also suggested by Bazilevskaya et al. (2015), bedrock chemical and physical characteristics might exert a strong control on the propagation rate of the weathering front and hence on denudation rates. For example, as bedrock Fe concentrations are low at our site (compared to mafic rocks), micro-cracks produced during oxidation reactions can form at a rate slower than in bedrocks with higher Fe content, resulting in slower weathering zone propagation. In charnockite, porosity and connected internal surface area of grain boundaries and micro-fractures are below the detection limit of the BET method and He pycnometry. In the case of this coherent bedrock it appears that almost no internal surfaces are available in the bedrock which could provide contact between minerals and reactive phases.

A second explanation for these low rates stems from the coupling between the weathering zone advance rate and the O_2 concentration, which at depth is dependent on the regolith thickness (Buss et al., 2008) and on the type of transport of fluids permitted by the regolith, as shown in section 4.3 above. In thick tropical weathering profiles such as those encountered at Hakgala, weathering processes themselves can influence the type of fluid transport. Hydraulic conductivities K_s less than 0.08 cm/h were observed by Lohse and Dietrich (2005) to occur in lower parts of old soils (> 20 cm below the surface) where clay layers hinder the infiltration and shallow sub-surface flows are established. The old soils, mainly composed of kaolinite, and Fe- and Al-(hydr)oxides, show decreasing K_s with high clay contents (Lohse and Dietrich, 2005). Because our results also reveal significant amounts of clay minerals and (non)crystalline Fe- and Al- (oxy)(hydr)oxides in the regolith, it is reasonable to infer low hydraulic conductivity throughout the profile at Hakgala. Moreover, overall mass transfer coefficients for Al and Fe ($\tau_{Al,\ Fe}$) are near zero (Hewawasam et al., 2013). Hence, many of the secondary minerals that precipitated from amorphous precursors remain in the profile rather than being dissolved. Therefore, they might maintain the low permeability at least in the lower part of the profile. When such a thick profile is present, only mechanical disruption by erosion processes might form preferential pathways for fluids and O_2. Such processes are not active at Hakgala because of the absence of tectonically driven landscape rejuvenation (*e.g.,* von Blanckenburg et al., 2004). The lack of local base level lowering by tectonic movements results in long-term stability of the drainage pattern, leading to low erosion rates (Edmond et al., 1995). In addition to tectonic activity, the dense natural vegetation cover exerts a strong control over erosion rate (Istanbulluoglu, 2005; Kirkby, 1995; Vanacker et al., 2007a). During monsoon the soil surface is shielded from rain by the canopy, lowering the velocities of the drops and reducing rain-splash at the surface. Tree leaves also increase evapotranspiration, thereby reducing the amount of rain that reaches the soil surface. Additionally, the roots of the plants stabilize the soil, decreasing mass movement (Gyssels et al., 2005). Therefore, erosion at the surface is reduced by the dense vegetation cover prevailing up to large-scale deforestation (Hewawasam et al., 2003).

The combination of these effects that all stabilize the mobile layer provide the conditions to accumulate a thick regolith that slows weathering at depth, until steady-state is reached and low rates of erosion and weathering front advance match. This results in the "soil-shielding" effect where the thick regolith acts as a protecting layer, shielding the bedrock from weathering. Although steady-state is actually observed at Hakgala, we note that in settings where even deeper regolith might form the advance of the weathering front might be totally decoupled from erosion at the surface and regolith might accumulate (Lebedeva et al., 2010). Interestingly, our weathering profile at Hakgala fits well with the observation made by Bazilevskaya et al (2013) that slow weathering profiles developed on granitoid lithology obtain similar thicknesses of mostly 10 – 20 m.

At this point, we would like to stress why we consider the "top down" control over the weathering-erosion feedback illustrated and quantified in detail in this paper rather than exploring the approach of Rempe and Dietrich (2014). In this alternative model the advance of the weathering front is driven by fluid flow when bedrock enters the saturated zone as driven by channel incision. A requirement is that the bedrock entering the weathering zone features a porosity that provides pathways for reacting fluids. However, the bedrock at the Hakgala regolith profile in Sri Lanka is relatively compact and does not show any connected porosity. Hence, porosity and fractures must first be produced to provide the hydraulic conductivity required to saturate the bedrock with fluids. Therefore we consider surface-controlled O_2 driven fracturing to be the rate-limiting step that results in a connection between erosion at the surface and weathering at depth.

5. Conclusions

From the observations at the Hakgala weathering profile in the Central Highlands of Sri Lanka we propose that: (1) The first process initiating weathering of low-porosity charnockite at depth is oxidation of Fe(II)-bearing primary minerals. The oxidation produces micro-cracks due to a positive volume budget. The micro-cracks allow percolation of reactive fluids, promoting further weathering reactions and the subsequent dissolution of plagioclase. (2) During weathering a distinct opening of porosity occurs which further increases the access of reactive phases, and dissolution of plagioclase is enhanced producing a narrow rindlet zone where bedrock is converted into saprolite. (3) Weathering of primary minerals first leads to an amorphous precursor from which secondary clay minerals and crystalline oxides form. This finding is important regarding the implementation of reactive transport models at the scale of soil columns, especially in terms of numerical parameters representing secondary phase solubilities and formation rates. (4) The supply of O_2 acts as the main feedback mechanism and the consumption of O_2 at depth is coupled to the supply of atmospheric O_2, which in turn is controlled by erosion at the top of the profile. Therefore, we conclude that O_2 supply is the rate-limiting factor for weathering advance, and the type of O_2 transport through the regolith influences the strength of this feedback. (5) Re-addressing the questions raised in the introduction: low chemical weathering rates and stable saprolite profiles are promoted on lithologies with low porosity and a low

concentration of Fe(II)-bearing primary minerals. Such lithology is prevalent at our Hakgala site in the form of high-grade metamorphosed charnockite. Furthermore, we point out that low chemical weathering rates are promoted in (a) tectonically quiescent regions (like the Central Highlands of Sri Lanka), where the bedrock and the saprolite profile are not deformed by tectonic activity and hence, less preferential fluid pathways form; and (b) regions of dense natural vegetation cover which decreases the amount of rainwater reaching the surface and stabilizes the surface with their roots with respect to erosion. Both influence the regolith transport properties on hill slopes in such a way that the weathering front propagation rate remains low.

Acknowledgements: Stefan Gehrmann and Otto Diedrich are thanked for preparation of cylindrical samples from the corestone, and Tobias Meier and Eric Rybacki for their guidance with the He-pycnometry measurements. Thanks also go to Michael Klatt for support of laboratory work in Hannover, to Franziska Adams for help with Fe-redox analyses, and to Jean L. Dixon for sampling support. Dieter Rhede is acknowledged for electron microprobe analytical support and Geerke Floor and anonymous reviewers for comments on this manuscript. This work was conducted in the frame of the Graduate School GRK1364 funded by the German Science Foundation (DFG), co-financed by GFZ Potsdam, and the University of Potsdam.

APPENDIX A. Supplementary data

Supplementary data to this article can be found online at http://dx.doi.org/10.1016/j.chemgeo.2015.07.008.

References:

Balan, E., 2006. First-principles study of the OH-stretching modes of gibbsite. American Mineralogist 91, 115-119.

Bazilevskaya, E., Lebedeva, M., Pavich, M., Rother, G., Parkinson, D.Y., Cole, D., Brantley, S.L., 2013. Where fast weathering creates thin regolith and slow weathering creates thick regolith. Earth Surface Processes and Landforms 38, 847-858.

Bazilevskaya, E., Rother, G., Mildner, D.F.R., Pavich, M., Cole, D., Bhatt, M.P., Jin, L., Steefel, C.I., Brantley, S.L., 2015. How Oxidation and Dissolution in Diabase and Granite Control Porosity during Weathering. Soil Science Society of America Journal 79, 55.

Bonneville, S., Smits, M.M., Brown, A., Harrington, J., Leake, J.R., Brydson, R., Benning, L.G., 2009. Plant-driven fungal weathering: Early stages of mineral alteration at the nanometer scale. Geology 37, 615-618.

Brady, N.C., Weil, R. R., 2007. The nature and properties of soils. 14th ed. Prentice Hall, Upper Saddle River, NJ.

Brantley, S.L., Bandstra, J., Moore, J., White, A.F., 2008. Modelling chemical depletion profiles in regolith. Geoderma 145, 494-504.

Brantley, S.L., Lebedeva, M., 2011. Learning to Read the Chemistry of Regolith to Understand the Critical Zone. Annual Review of Earth and Planetary Sciences 39, 387-416.

Braun, J.-J., Descloitres, M., Riotte, J., Fleury, S., Barbiéro, L., Boeglin, J.-L., Violette, A., Lacarce, E., Ruiz, L., Sekhar, M., Mohan Kumar, M.S., Subramanian, S., Dupré, B., 2009. Regolith mass balance inferred from combined mineralogical, geochemical and geophysical studies: Mule Hole gneissic watershed, South India. Geochimica et Cosmochimica Acta 73, 935-961.

Braun, J.-J., Marechal, J.-C., Riotte, J., Boeglin, J.-L., Bedimo Bedimo, J.-P., Ndam Ngoupayou, J.R., Nyeck, B., Robain, H., Sekhar, M., Audry, S., Viers, J., 2012. Elemental weathering fluxes and

saprolite production rate in a Central African lateritic terrain (Nsimi, South Cameroon). Geochimica et Cosmochimica Acta 99, 243-270.
Bray, A.W., Benning, L.G., Bonneville, S., Oelkers, E.H., 2014. Biotite surface chemistry as a function of aqueous fluid composition. Geochimica et Cosmochimica Acta 128, 58-70.
Brimhall, G.H., Dietrich, W.E., 1987. Constitutive mass balance relations between chemical composition, volume, density, porosity, and strain in metasomatic hydrochemical systems: Results on weathering and pedogenesis. Geochimica et Cosmochimica Acta 51, 567-587.
Brunauer, S., Emmett, P.H., Teller, E., 1938. Adsorption of Gases in Multimolecular Layers. Journal of the American Chemical Society 60, 309-319.
Buss, H.L., Sak, P.B., Webb, S.M., Brantley, S.L., 2008. Weathering of the Rio Blanco quartz diorite, Luquillo Mountains, Puerto Rico: Coupling oxidation, dissolution, and fracturing. Geochimica et Cosmochimica Acta 72, 4488-4507.
Carson, M.A., Kirkby, M.J., 1972. Hillslope form and process. Cambridge University Press, , New York.
Chadwick, O.A., Chorover, J., 2001. The chemistry of pedogenic thresholds. Geoderma 100, 321-353.
Colin, F., Nahon, D., Trescases, J.J., Melfi, A.J., 1990. Lateritic Weathering of Pyroxenites at Niquelandia, Goias, Brazil: The Supergene behavior of Nickel. Economic Geology 85, 1010-1023.
Dahlgren, R.A., Boettinger, J.L., Huntington, G.L., Amundson, R.G., 1997. Soil development along an elevational transect in the western Sierra Nevada, California. Geoderma 78, 207-236.
Delvigne, J., 1983. Micromorphology of the alteration and weathering of pyroxenes in the Koua Bocca ultramafic intrusion, Ivory Coast, Western Africa. Sci. Géol., Mém. 72, 57-68.
Dequincey, O., Chabaux, F., Clauer, N., Liewig, N., Muller, J., 1999. Dating of weathering profiles by radioactive disequilibria: contribution of the study of authigenic mineral fractions. Comptes Rendus de l'Academie des Sciences Series IIA Earth and Planetary Science 328, 679-685.
Dixon, J.L., von Blanckenburg, F., 2012. Soils as pacemakers and limiters of global silicate weathering. Comptes Rendus Geoscience 344, 597-609.
Dong, H., Peacor, D.R., Murphy, S.F., 1998. TEM study of progressive alteration of igneous biotite to kaolinite throughout a weathered soil profile. Geochimica et Cosmochimica Acta 62, 1881-1887.
Edmond, J.M., Palmer, M.R., Measures, C.I., Grant, B., Stallard, R.F., 1995. The fluvial geochemistry and denudation rate of the Guyana Shield in Venezuela, Colombia, and Brazil. Geochimica et Cosmochimica Acta 59, 3301-3325.
Fletcher, R., Buss, H., Brantley, S., 2006. A spheroidal weathering model coupling porewater chemistry to soil thicknesses during steady-state denudation. Earth and Planetary Science Letters 244, 444-457.
Foster, M.D., 1953. The determination of free silica and free alumina in montmorillonites. Geochmica et Cosmochimica Acta 3, 143-154.
Goddéris, Y., Donnadieu, Y., Tombozafy, M., Dessert, C., 2008. Shield effect on continental weathering: Implication for climatic evolution of the Earth at the geological timescale. Geoderma 145, 439-448.
Goddéris, Y., François, L.M., Probst, A., Schott, J., Moncoulon, D., Labat, D., Viville, D., 2006. Modelling weathering processes at the catchment scale: The WITCH numerical model. Geochimica et Cosmochimica Acta 70, 1128-1147.
Gunnell, Y., Louchet, A., 2000. The influence of rock hardness and divergent weathering on the interpretation of apatite fission-track denudation rates. Evidence from charnockites in South India and Sri Lanka. Zeitschrift Geomorphologie N. F. 44, 33-57.
Gustafsson, J.P., Bhattacharya, P., Karltun, E., 1999. Mineralogy of poorly crystalline aluminum phases in the B horizon of Podzols in southern Sweden. Applied Geochemistry 14, 707-718.
Gyssels, G., Poesen, J., Bochet, E., Li, Y., 2005. Impact of plant roots on the resistance of soils to erosion by water: a review. Progress in Physical Geography 29, 189-217.
Hartmann, J., Moosdorf, N., Lauerwald, R., Hinderer, M., West, A.J., 2014. Global chemical weathering and associated P-release — The role of lithology, temperature and soil properties. Chemical Geology 363, 145-163.
Heimsath, A.M., Dietrich, W.E., Nishiizumi, K., Finkel, R.C., 1997. The soil production function and landscape equilibrium. Nature 388, 358-361.

Heimsath, A.M., Fink, D., Hancock, G.R., 2009. The 'humped' soil production function: eroding Arnhem Land, Australia. Earth Surface Processes and Landforms 34, 1674-1684.
Hellmann, R., Wirth, R., Daval, D., Barnes, J.-P., Penisson, J.-M., Tisserand, D., Epicier, T., Florin, B., Hervig, R.L., 2012. Unifying natural and laboratory chemical weathering with interfacial dissolution–reprecipitation: A study based on the nanometer-scale chemistry of fluid–silicate interfaces. Chemical Geology 294-295, 203-216.
Hewawasam, T., von Blanckenburg, F., Bouchez, J., Dixon, J.L., Schuessler, J.A., Maekeler, R., 2013. Slow advance of the weathering front during deep, supply-limited saprolite formation in the tropical Highlands of Sri Lanka. Geochimica et Cosmochimica Acta 118, 202-230.
Hewawasam, T., von Blanckenburg, F., Schaller, M., Kubik, P., 2003. Increase of human over natural ersosion rates in tropical highlands constrained by cosmogenic nuclides. Geology 31, 597-600.
Hong, H., Churchman, G.J., Gu, Y., Yin, K., Wang, C., 2012. Kaolinite–smectite mixed-layer clays in the Jiujiang red soils and their climate significance. Geoderma 173-174, 75-83.
Hong, H., Li, Z., Xiao, P., 2009. Clay mineralogy along the laterite profile in Hubei, South China: mineral evolution and evidence for eolian origin. Clays and Clay Minerals 57, 602-615.
Istanbulluoglu, E., 2005. Vegetation-modulated landscape evolution: Effects of vegetation on landscape processes, drainage density, and topography. Journal of Geophysical Research 110, 1-19.
Jamtveit, B., Kobchenko, M., Austrheim, H., Malthe-Sørenssen, A., Røyne, A., Svensen, H., 2011. Porosity evolution and crystallization-driven fragmentation during weathering of andesite. Journal of Geophysical Research 116, 1-12.
Jamtveit, B., Putnis, C.V., Malthe-Sørenssen, A., 2008. Reaction induced fracturing during replacement processes. Contributions to Mineralogy and Petrology 157, 127-133.
Kalinowski, B.E., Schweda, P., 1996. Kinetics of muscovite, phlogopite, and biotite dissolution and alteration at pH 1-4, room temperature. Geochimica et Cosmochimica Acta 60, 367 385.
Kirkby, M., 1995. Modelling the links between vegetation and landforms. Geomorphology 13, 319-335.
Kourkoumelis, N., 2013. PowDLL: A program for the interconversion of powder diffraction data files, University of Ioannina, Greece. http://users.uoi.gr/nkourkou/powdll/.
Lebedeva, M.I., Fletcher, R.C., Balashov, V.N., Brantley, S.L., 2007. A reactive diffusion model describing transformation of bedrock to saprolite. Chemical Geology 244, 624-645.
Lebedeva, M.I., Fletcher, R.C., Brantley, S.L., 2010. A mathematical model for steady-state regolith production at constant erosion rate. Earth Surface Processes and Landforms, 508-524.
Lohse, K.A., Dietrich, W.E., 2005. Contrasting effects of soil development on hydrological properties and flow paths. Water Resources Research 41, 1-17.
Ma, L., Chabaux, F., Pelt, E., Granet, M., Sak, P.B., Gaillardet, J., Lebedeva, M., Brantley, S.L., 2012. The effect of curvature on weathering rind formation: Evidence from Uranium-series isotopes in basaltic andesite weathering clasts in Guadeloupe. Geochimica et Cosmochimica Acta 80, 92-107.
Maher, K., Steefel, C.I., White, A.F., Stonestrom, D.A., 2009. The role of reaction affinity and secondary minerals in regulating chemical weathering rates at the Santa Cruz Soil Chronosequence, California. Geochimica et Cosmochimica Acta 73, 2804-2831.
Malmström, M., Banwart, S., 1997. Biotite dissolution at 25°C: The pH dependence of dissolution rate and stoichiometry. Geochimica et Cosmochimica Acta 61, 2779-2799.
Mayes, M.A., Jardine, P.M., Mehlhorn, T.L., Bjornstad, B.N., Ladd, J.L., Zachara, J.M., 2003. Transport of multiple tracers in variably saturated humid region structured soils and semi-arid region laminated sediments. Journal of Hydrology 275, 141-161.
Mehra, O.P., Jackson, M.L., 1960. Iron oxides removal from soils and clays by a dithionite-citrate system buffered with sodium bicarbonate. Clays and Clay Minerals, Proceedings of the 7th National Conference, 317-327.
Merino, E., Nahon, D., Wang, Y., 1993. Kinetics and mass transfer of pseudomorphic replacement: Application to replacement of parent minerals and kaolinite by Al, Fe, and Mn oxides during weathering. American Journal of Science 293, 135-155.
Moore, D.M., Reynolds, R.C.J., 1997. X-Ray Diffraction and the Identification and Analysis of Clay Minerals, 2 ed. Oxford University Press, Inc., New York.
Moore, J., Lichtner, P.C., White, A.F., Brantley, S.L., 2012. Using a reactive transport model to elucidate differences between laboratory and field dissolution rates in regolith. Geochimica et Cosmochimica Acta 93, 235-261.

Murphy, S.F., Brantley, S.L., Blum, A.E., White, A.F., Dong, H., 1998. Chemical weathering in a tropical watershed, Luquillo Mountains, Puerto Rico: II. Rate and mechanism of biotite weathering. Geochimica et Cosmochimica Acta 62, 227-243.

Navarre-Sitchler, A., Steefel, C.I., Sak, P.B., Brantley, S.L., 2011. A reactive-transport model for weathering rind formation on basalt. Geochimica et Cosmochimica Acta 75, 7644-7667.

Navarre-Sitchler, A.K., Cole, D.R., Rother, G., Jin, L., Buss, H.L., Brantley, S.L., 2013. Porosity and surface area evolution during weathering of two igneous rocks. Geochimica et Cosmochimica Acta 109, 400-413.

Noack, Y., Colin, F., Nahon, D., Delvigne, J., Michaux, L., 1993. Secondary-mineral formation during natural weathering of pyroxene: Review and thermodynamic approach. American Journal of Science 293, 111-134.

Palacio, L., Prádanos, P., Calvo, J.I., Hernández, A., 1999. Porosity measurements by a gas penetration method and other techniques applied to membrane characterization. Thin Solid Films 348, 22-29.

Rempe, D.M., Dietrich, W.E., 2014. A bottom-up control on fresh-bedrock topography under landscapes. PNAS 111, 6576-6581.

Riebe, C.S., Kirchner, J.W., Finkel, R.C., 2003. Long-term rates of chemical weathering and physical erosion from cosmogenic nuclides and geochemical mass balance. Geochimica et Cosmochimica Acta 67, 4411-4427.

Robert, C., Kennett, J.P., 1994. Antartic subtropical humid episode at the Paleocene-Eocene boundary: Clay mineral evidence. Geology 22, 211-214.

Robie, R.A., Hemingway, B.S., 1995. Thermodynamic Properties of Minerals and Related Substances at 298.15 K and 1 Bar (10^5 Pascals) Pressure and at Higher Temperatures. U. S. Geological Survey Bulletin, Washington.

Røyne, A., Jamtveit, B., Mathiesen, J., Malthe-Sørenssen, A., 2008. Controls on rock weathering rates by reaction-induced hierarchical fracturing. Earth and Planetary Science Letters 275, 364-369.

Rudge, J.F., Kelemen, P.B., Spiegelman, M., 2010. A simple model of reaction-induced cracking applied to serpentinization and carbonation of peridotite. Earth and Planetary Science Letters 291, 215-227.

Sak, P.B., Fisher, D.M., Gardner, T.W., Murphy, K., Brantley, S.L., 2004. Rates of weathering rind formation on Costa Rican basalt. Geochimica et Cosmochimica Acta 68, 1453-1472.

Sak, P.B., Navarre-Sitchler, A.K., Miller, C.E., Daniel, C.C., Gaillardet, J., Buss, H.L., Lebedeva, M.I., Brantley, S.L., 2010. Controls on rind thickness on basaltic andesite clasts weathering in Guadeloupe. Chemical Geology 276, 129-143.

Sauer, D., Saccone, L., Conley, D.J., Herrmann, L., Sommer, M., 2006. Review of methodologies for extracting plant-available and amorphous Si from soils and aquatic sediments. Biogeochemistry 80, 89-108.

Schuessler, J.A., Botcharnikov, R.E., Behrens, H., Misiti, V., Freda, C., 2008. Oxidation state of iron in hydrous phono-tephritic melts. American Mineralogist 93, 1493-1504.

Schwertmann, U., 1964. Differenzierung der Eisenoxide des Bodens durch Extraktion mit Ammoniumoxaltat-Lösung. Zeitschrift für Pflanzenernährung, Düngung, Bodenkunde 105, 194-202.

Shelobolina, E., Xu, H., Konishi, H., Kukkadapu, R., Wu, T., Blothe, M., Roden, E., 2012. Microbial lithotrophic oxidation of structural Fe(II) in biotite. Applied and environmental microbiology 78, 5746-5752.

Stallard, R.F., 1995. Tectonic, Environmental, and Human Aspects of Weathering and Erosion: A Global Review using a Steady-State Perspective. Annu. Rev. Earth Planet. Sci 23, 11-39.

Steefel, C.I., van Cappellen, P., 1990. A new kinetc approach to modeling water-rock interaction: The role of nucleation, precursors, and Ostwald ripening. Geochimica et Cosmochimica Acta 54, 2657-2677.

van der Marel, H.W., Beutelspacher, H., 1976. Atlas of Infrared Spectroscopy of Clay Minerals and their Admixtures. Elsevier Scientific Publishing Company.

Vanacker, V., von Blanckenburg, F., Govers, G., Molina, A., Poesen, J., Deckers, J., Kubik, P., 2007a. Restoring dense vegetation can slow mountain erosion to near natural benchmark levels. Geology 35, 303-306.

Vanacker, V., von Blanckenburg, F., Hewawasam, T., Kubik, P.W., 2007b. Constraining landscape development of the Sri Lankan escarpment with cosmogenic nuclides in river sediment. Earth and Planetary Science Letters 253, 402-414.

Velbel, M.A., 1993. Formation of protective surface layers during silicate-mineral weathering under well-leached, oxidizing conditions. American Mineralogist 78, 405-414.

von Blanckenburg, F., Hewawasam, T., Kubik, P.W., 2004. Cosmogenic nuclide evidence for low weathering and denudation in the wet, tropical highlands of Sri Lanka. Journal of Geophysical Research 109, 1-22.

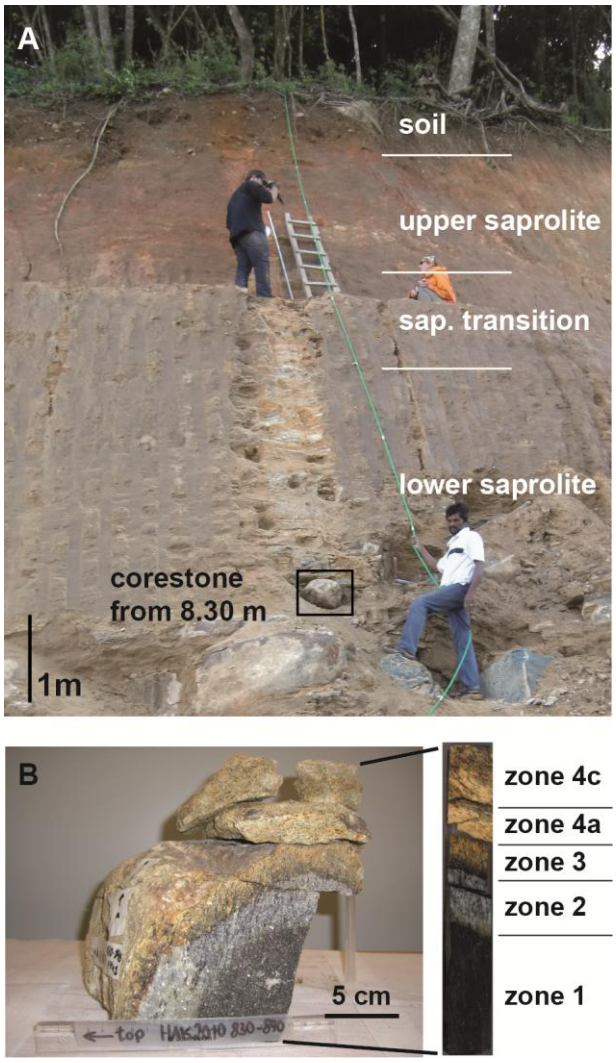

Figure 1 Study site. Photographs of the regolith profile (A) and the investigated corestone from 830 cm depth (B). The corestone was sampled from the approximately 3 m-thick corestone zone in the lower part of the profile. The polished section shown in (B) was prepared from this corestone and shows the different weathered zones in detail.

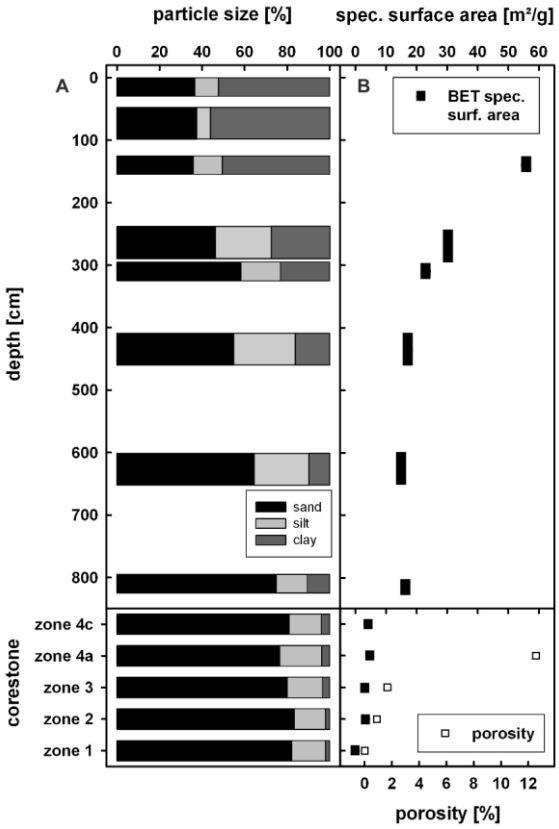

Figure 2 Textural results from the Hakgala profile. (A) particle size analyses. (B) specific surface area (SSA, upper axis) analyzed by the N_2 adsorption method, and porosity (lower axis). The upper section represents the saprolite and soil and the lower section the different corestone zones. Note that in the dense corestone the BET method gives the connected internal surface area, which is below detection limit for corestone zone 1 (Table 1). Porosity measurements were conducted for the corestone only. Error bars are smaller than the symbols.

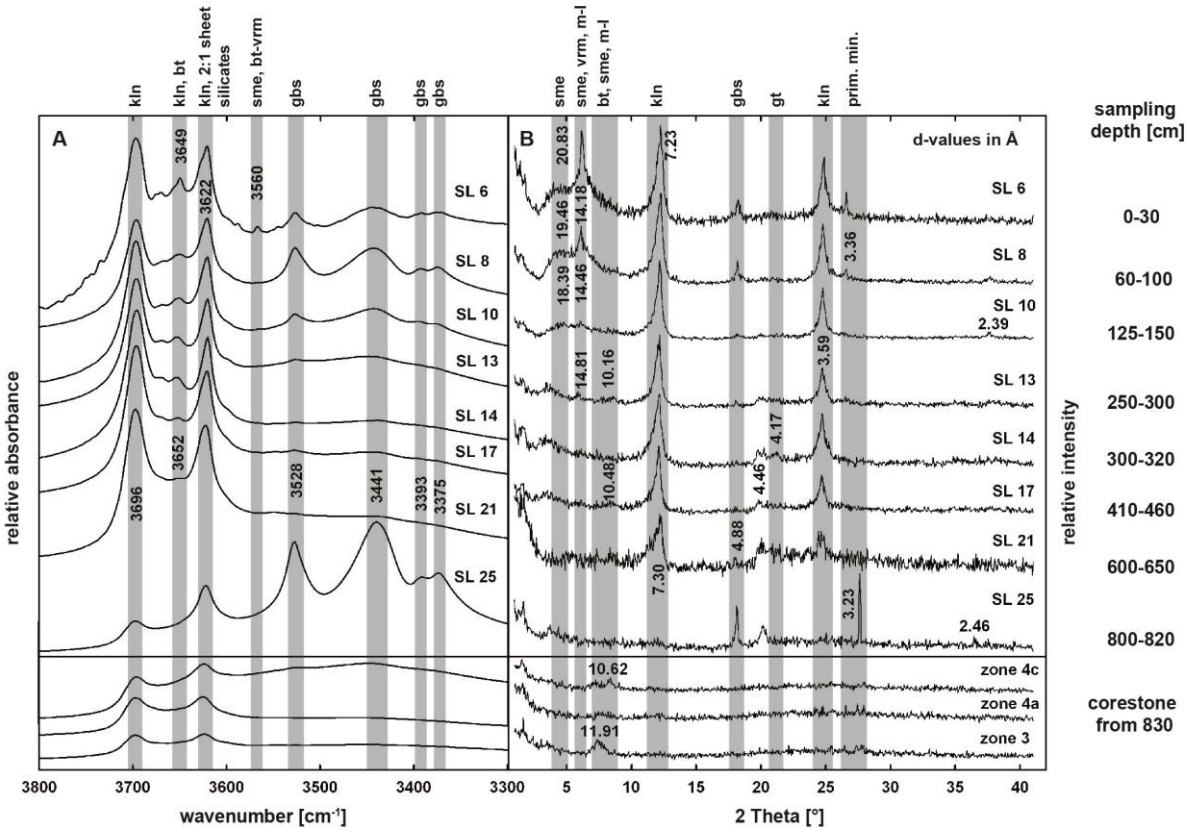

Figure 3 Results of IR spectroscopy (A) and X-ray diffraction (B) measurements on clay-sized fractions separated from the regolith samples and the corestone. Because the clay-sized fractions of corestone zones 1 and 2 are dominated by primary minerals spectra for these zones are not shown. The IR spectra in (A) are only shown from 3800 to 3300 cm^{-1} to facilitate the identification of secondary minerals according to their OH-stretching vibrations. The labeled d-spacing values in the XRD pattern (B) are reported in Å units. The primary mineral peaks at 3.36 and 3.23 Å are quartz and feldspar, respectively. bt: biotite, gbs: gibbsite, gt: goethite, kln: kaolinite, m-l: mixed-layer clays, sme: smectite, vrm: vermiculite.

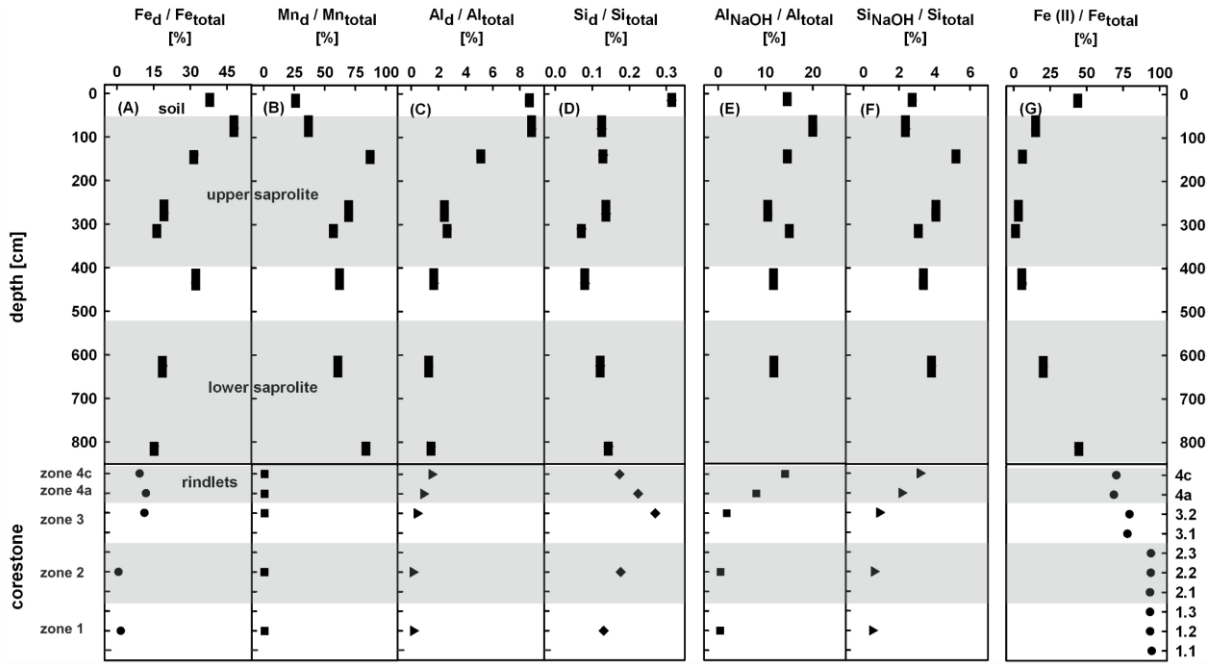

Figure 4 Results of the selective extractions. (A-D) Fractions [%] of Fe, Mn, Al, and Si contained in Fe-amorphous phases and Fe-(oxy)(hydr)oxides (extracted using dithionite). (E, F) Fractions [%] of Al and Si contained in Al-amorphous phases (extracted using NaOH). The total concentration of each element in the bulk sample was measured by XRF (data from Hewawasam et al., 2013). (G) Fe(II) / Fe_{total} ratio. The gray horizontal bands indicate different zones in the saprolite, and the corestone. Error bars are smaller than the symbols. The Mn_d contents in the corestone dithionite extractions were below detection limit (Table 1) and hence Mn_d/Mn_{total} are plotted close to zero in the lower section of panel B for illustrative purposes.

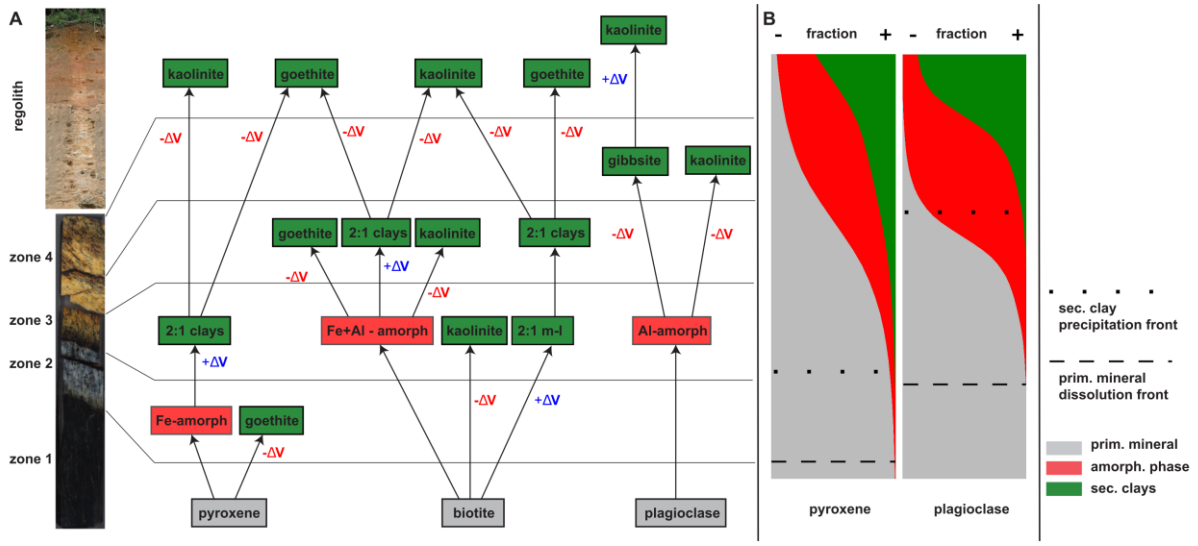

Figure 5 Sketch of the pathways of mineral reactions during weathering of pyroxene, biotite, and plagioclase (A). Specific volume increase is presented in blue (+ΔV), and decreasing volume is presented in red (-ΔV). Volume changes during these reactions are associated with conversion to crystalline secondary products (green boxes). Meta-stable amorphous precursors are indicated by red boxes. For some reactions, especially those involving amorphous secondary phases, specific volume changes are not known. Fe-(oxy)(hydr)oxides are indicated as goethite, which was identified by XRD. Mixed layer clays (m-l clays) include combination of biotite with secondary 2:1 clay minerals such as smectite, vermiculite, or hydrobiotite. Panel B schematically shows the onset of weathering for pyroxene and plagioclase at the weathering front (dashed horizontal line: primary mineral dissolution front) and the conversion of amorphous secondary phases to crystalline secondary clay minerals (dotted horizontal line: secondary clay crystallization front) in the corestone and the lower saprolite. As the reactions shown in panel A are continuously taking place in the corestone and the rindlets, (non)crystalline Fe- Al-(oxy)(hydr)oxides appear also in the upper part of the graph in panel B. (For interpretation of the reference to color in this figure legend, the reader is referred to the web version of this article).

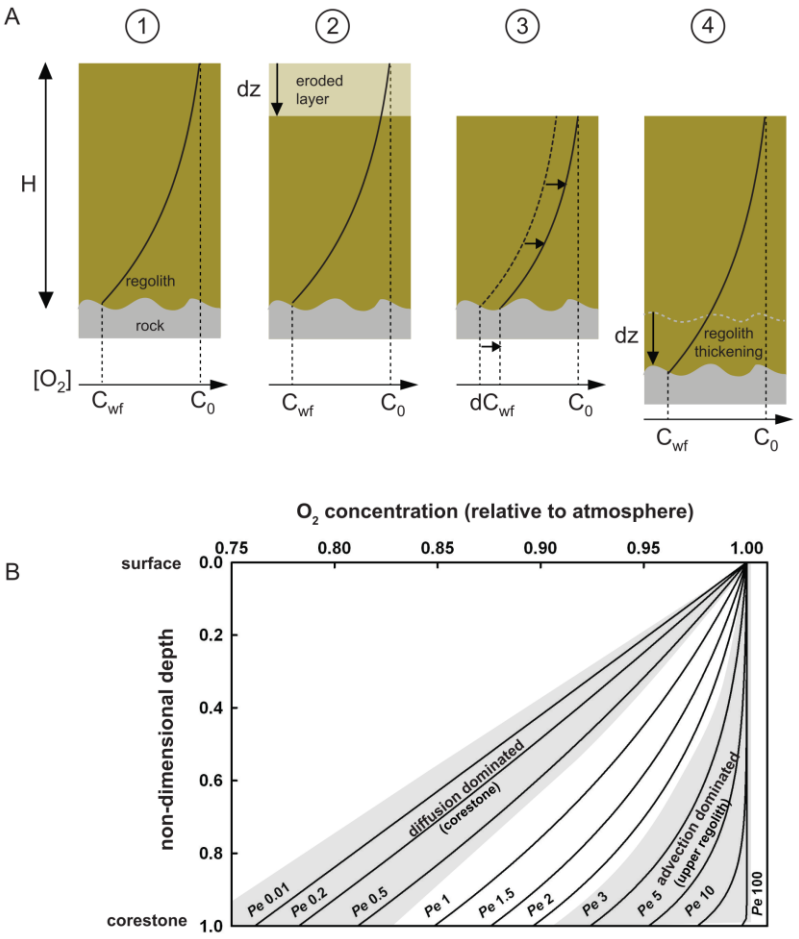

Figure 6 (A) Conceptual sketch showing how the coupling between regolith thickness and transport properties can be linked with the propagation of the weathering front through a feedback (Fletcher et al., 2006) for a given O_2 concentration profile. The O_2 profiles are modeled with respect to the consumption of O_2 due to oxidation of pyroxene and biotite at depth in the Hakgala weathering profile. (1) Initial steady state: the regolith thickness is *H*, the O_2 concentration in the pore and fracture network is C_0 (atmospheric concentration) at the surface and C_{wf} at the weathering front, with $C_{wf} < C_0$ as O_2 is consumed by oxidative weathering reactions at the weathering front. (2) An infinitesimal erosion event removes a layer of thickness *dz* at the regolith surface, which pushes the system out of steady state. (3) Re-equilibration of O_2 at the surface with the atmosphere results in an increase of O_2. As the transport properties of the regolith are not modified by the erosion event itself, the O_2 gradient throughout the regolith remains the same, such that C_{wf} increases too by an infinitesimal amount dC_{wf}. (4) The increase in C_{wf} enhances the kinetics of oxidative weathering reactions, ensuing fracturing and downward propagation of the weathering front by a distance *dz*, resulting in regolith thickening until the concentration of O_2 at the weathering front is C_{wf} again. The system is back at steady state. The "speed" at which the downward propagation of the weathering front occurs after the erosion event, which reflects the "strength" of the feedback, is set by the value of dC_{wf} for a given *dz*, *i.e.*, by the gradient of O_2 concentration in the lowest part of the regolith (Fletcher et al., 2006), which is in turn dependent on the type of transport prevailing in the regolith (advective *vs.* diffusive). (B) Modeled O_2 concentration profiles as a function of the Péclet number (*Pe*): normalized O_2 concentrations in the profile versus normalized depth at different Péclet numbers. The O_2 concentration profiles are directly related to the consumption of O_2 at depth, calculated here using our data from the Hakgala weathering profile. The O_2 consumption depends on the oxidation of pyroxene and biotite in the corestone and the rindlets, which we quantified in the 3-m-thick corestone zone. Although for this simple model we assumed that one *Pe* number applies to the whole weathering profiles, low *Pe* numbers might be characteristic of transport in the corestone, and high *Pe* numbers characteristic of transport in the saprolite.

Table 1 Compilation of measurement results in corestone and regolith samples.

sample[a]		depth	particle size distribution			SSA[b]	porosity	selective extractions[c]							Fe(II)/ Fe_{total}
			sand	silt	clay			Fe_d/Fe_{total}	Mn_d/Mn_{total}	Al_d/Al_{total}	Al_{NaOH}/Al_{total}	Si_d/Si_{total}	Si_{NaOH}/Si_{total}	Σ_{d+NaOH}	
		[cm]	[%]	[%]	[%]	[m^2/g]	[vol%]	[%]	[%]	[%]	[%]	[%]	[%]	[wt.%]	[%]
soil															
	SL 6	0 – 30	36.6	11.1	52.3			37.8	25.7	8.6	14.6	0.3	2.7	9.7	44
upper saprolite															
	SL 8	60 – 100	37.4	6.6	56.0			47.9	36.2	8.8	20.1	0.1	2.3	13.6	15
	SL 10	125 – 150	35.9	13.7	50.4	55.6		31.5	87.4	5.0	14.8	0.1	5.1	13.6	6
	SL 13	250 – 300	46.1	26.7	27.2	30.2		19.3	69.6	2.3	10.6	0.1	4.0	8.4	3
	SL 14	300 – 320	58.2	18.7	23.2	23.2		16.2	57.4	2.6	15.1	0.1	3.0	6.6	1
transition zone															
	SL 17	410 – 460	54.7	29.3	16.0	17.3		32.0	61.7	1.6	11.7	0.1	3.3	7.2	6
lower saprolite															
	SL 21	600 – 650	64.4	26.1	9.6	15.1		18.8	60.1	1.2	11.9	0.1	3.8	6.5	20
	SL 25	800 – 820	74.8	14.7	10.5	16.6		15.3	83.8	1.4		0.1			44
corestone															
zone 4	4c	corestone from 830 cm depth	80.9	15.2	3.9	4.0		9.2	< 0.05 [d]	1.5	14.2	0.2	3.2	5.3	70
	4a		76.6	19.6	3.8	4.7	12.6	11.8	< 0.05 [d]	0.9	8.1	0.2	2.2	3.6	68
zone 3	3.2		80.1	16.6	3.3	3.1	1.66	11.2	< 0.05 [d]	0.4	1.8	0.3	0.9	1.5	79
	3.1														78
zone 2	2.3		83.4	14.7	2.0	3.4	0.89	0.6	< 0.05 [d]	0.1	0.5	0.2	0.6	0.6	94
	2.2														94
	2.1														93
zone 1	1.3		82.2	15.9	2.0	< 0.01[d]	ϕ_{pore} < He [d]	1.5	< 0.05 [d]	0.1	0.5	0.1	0.5	0.6	93
	1.2														93
	1.1														94

[a]See figure 1 for sampling in the regolith profile and corestone.
[b]SSA is the specific surface area of bulk samples determined from N_2 adsorption. For the corestone this represents the connected internal surface area.
[c]Extractions were performed on bulk samples using dithionite (d) and NaOH to release elements from Fe-amorphous phases, (Fe-hydr)oxides and Al-Si-amorphous phases, respectively. Leached element fractions are reported relative to the total element concentration in the bulk sample in percent. The sum of the dithionite- and NaOH-extractable phases given in oxide wt.% of the bulk sample gives an upper limit as both leaching methods (dithionite and NaOH) partly extract both (Fe- and Al-) phases.
[d]below detection limit.

Table 2 Secondary mineral associations of the < 2 µm fraction in regolith profile and corestone.

zone	sample	depth [cm]	minerals in < 2 µm size fraction
soil	SL 6	0 – 30	kaolinite, 2:1 clays, gibbsite
upper saprolite	SL 8	60 – 100	kaolinite, 2:1 clays, gibbsite,
	SL 10	125 – 150	kaolinite, gibbsite, (2:1 clays)
	SL 13	250 – 300	kaolinite, gibbsite, (2:1 clays)
	SL 14	300 – 320	kaolinite, goethite
transition zone	SL 17	410 – 460	kaolinite, goethite
lower saprolite	SL 21	600 – 650	kaolinite, gibbsite, goethite
	SL 25	800 – 820	kaolinite, gibbsite, goethite
corestone			
zone 4c	SL 55	corestone from 830 cm depth	kaolinite, gibbsite, 2:1 clays, goethite
zone 4a	SL 53		kaolinite, goethite, 2:1 clays
zone 3	SL 49		kaolinite, biotite, 2:1 clays, goethite
zone 2	SL 48b		(primary minerals), biotite, goethite, (2:1 clays)
zone 1	SL 48a		(primary minerals)

Table 3 Parameters for oxidation model calculations.

parameter	value	unit
$V_{Fe(OH)3}$	1.92×10^{-4}	m^3/kg
V_{FeO}	1.75×10^{-4}	m^3/kg
ρ_{rock}	2700	kg/m^3
$[px]_{rock}$	4	vol%
$[bt]_{rock}$	7	vol%
$[Fe]_{rock}$	0.0316	kg/kg_{rock}
$[FeO]_{px}$	0.33	kg/kg_{px}
$[FeO]_{bt}$	0.20	kg/kg_{bt}
$[Fe]_{px, 0}$	0.020	kg/kg_{rock}
$[Fe]_{bt, 0}$	0.014 – 0.017	kg/kg_{rock}
$[px]_0$	0.059	kg/kg_{rock}
$[bt]_0$	0.072 – 0.086	kg/kg_{rock}
$[Fe(OH)_3]_0$	0	kg/kg_{rock}
E	1.0×10^{12}	dyn/cm^2
ν	0.25	-
2Γ	4.0×10^{5}	dyn/cm^2

The rock parameters are taken from Hewawasam et al. (2013). E, ν and 2Γ are from Fletcher et al. (2006). $[Fe]_{px}$, $[Fe]_{bt}$, $[px]_0$, and $[bt]_0$ are calculated as explained in Appendix A: Electronic Annex. The values for $[bt]_0$, and $[Fe]_{bt}$, depend on the biotite density, therefore a range is calculated using an annite and a phlogopite specific density. Molar volumes of FeO and $Fe(OH)_3$ [m^3/mol] from Robie and Hemingway (1995) were converted to [m^3/kg].

Table 4 Mineral-specific molar weight, molar volume, and density.

	molar weight [kg/mol]	molar volume [m^3/mol]	density [kg/m^3]
px (ferrosilite)	2.64×10^{-1}	6.60×10^{-5}	4.00×10^{3}
bt (annite)	5.12×10^{-1}	1.54×10^{-4}	3.32×10^{3}
bt (phlogopite)	4.17×10^{-1}	1.50×10^{-4}	2.79×10^{3}
FeO (wustite)	6.89×10^{-2}	1.20×10^{-5}	5.72×10^{3}
$Fe(OH)_3$	1.07×10^{-1}	2.05×10^{-5}	5.22×10^{3}
Fe	5.59×10^{-2}	-	-

The mineral specific values used to calculate the amount of iron bearing mineral $[x]_0$ (Eq. S2, Appendix A: Electronic Annex) were taken from Robie and Hemingway (1995). The pyroxene specific parameters are given for a mineral formula with 6 O atoms.

Table 5 Mass transfer coefficients for pyroxene (τ_{px}) and biotite (τ_{bt}).

corestone	min τ_{bt}	max τ_{bt}	τ_{px}
zone 1	0.00	0.00	0.00
zone 2	0.00	0.00	-0.17
zone 3	-0.02	-0.13	-0.30
zone 4	-0.03	-0.17	-0.75

Mass transfer coefficients τ are used to calculate the extent of weathering for pyroxene and biotite ($[x]_j$ in Eq S4, Appendix A: Electronic Annex) and is used for calculation of $FeO_{lost,\,j}$ (Eq S5, Appendix A: Electronic Annex) and the total volume change $\Delta\tilde{V}$ (Eq. (5)). τ_{px} was inferred from τ_{Mn} (Hewawasam et al., 2013). No single element is specific for biotite weathering, therefore the calculated minimum and maximum biotite depletion in the different zones are used (from Hewawasam et al., 2013).

Table 6 Evolution of volume changes ΔV, elastic strain ε, and strain energy density U in the corestone zones for different biotite compositions.

	corestone zone	U [dyn/cm²]	ε	$\Delta\tilde{V}$ [m³/kg$_{rock}$]	ΔV^{px} [m³/kg$_{rock}$]	ΔV^{bt} [m³/kg$_{rock}$]	$\Delta V^{Fe(OH)3}$ [m³/kg$_{rock}$]
bt (annite)	zone 1	0	0	0	0	0	0
	zone 2	1.78×10^{5}	3.66×10^{-4}	4.06×10^{-7}	-5.80×10^{-7}	0	9.87×10^{-7}
	zone 3	6.22×10^{5} to 1.06×10^{6}	6.83×10^{-4} to 8.91×10^{-4}	7.59×10^{-7} to 9.90×10^{-7}	-1.02×10^{-6}	-5.99×10^{-8} to -3.90×10^{-7}	1.84×10^{-6} to 2.40×10^{-6}
	zone 4	3.72×10^{6} to 1.56×10^{7}	1.67×10^{-3} to 3.42×10^{-3}	1.86×10^{-6} to 3.81×10^{-6}	-2.56×10^{-6}	-8.99×10^{-8} to -5.10×10^{-7}	4.51×10^{-6} to 5.22×10^{-6}
bt (phlogopite) min	zone 1	0	0	0	0	0	0
	zone 2	1.78×10^{5}	3.66×10^{-4}	4.06×10^{-7}	-5.80×10^{-7}	0	9.87×10^{-7}
	zone 3	6.11×10^{5} to 9.67×10^{5}	6.77×10^{-4} to 8.52×10^{-4}	7.52×10^{-7} to 9.46×10^{-7}	-1.02×10^{-6}	-5.04×10^{-8} to -3.28×10^{-7}	1.83×10^{-6} to 2.30×10^{-6}
	zone 4	3.68×10^{6} to 1.50×10^{7}	1.66×10^{-3} to 3.36×10^{-3}	1.85×10^{-6} to 3.73×10^{-6}	-2.56×10^{-6}	-7.56×10^{-8} to -4.28×10^{-7}	4.48×10^{-6} to 5.08×10^{-6}

U is the strain energy density. U must overcome the fracture surface energy 2Γ to fracture the rock, which is calculated according to equation 3. $\Delta\tilde{V}$ is the total volume change during oxidation of Fe(II) relative to the unweathered (un-oxidized) bedrock. This $\Delta\tilde{V}$ can be separated in the contribution of FeO oxidation from pyroxene (ΔV^{px}), biotite (ΔV^{bt}), and precipitation ($\Delta V^{Fe(OH)3}$). bt is calculated for different molar volumes of biotite: in lack of precise volumes for biotite present in the corestone, molar volumes of annite and phlogopite were taken from Robie and Hemingway (1995) to calculate a range of volume increase by biotite Fe oxidation. The range of values given for zones 3 and 4 is due to different τ, as calculated in Hewawasam et al. 2013.

Table 7 End members of schematic mineral weathering pathways in the corestone.

primary mineral		secondary mineral
pyroxene (orthopyroxene)[a] $(Fe_{1.0}Mg_{0.8}Ca_{0.1})Si_{1.8}O_6$ molar volume[b]: 66.00 cm³/mol	→	**goethite** FeOOH molar volume[b]: 20.82 cm³/mol **2:1 clay minerals** $X(Y)_3(AlSi)_4O_{10}(OH)_2$ molar volume[b,c]: >150 cm³/mol
biotite[a] $K_{0.7}(Fe_{1.0}Mg_{0.8}Ti_{0.2})(Al_{1.1}Si_{2.7})O_{10}(OH)_2$ molar volume[b]: 149.65 – 154.30 cm³/mol	→	**goethite** FeOOH molar volume[b]: 20.82 cm³/mol **2:1 clay minerals** $X_{0.3}(Y)_3(AlSi)_4O_{10}(OH)_2$ molar volume[b,c]: 150 – 577 cm³/mol **kaolinite** $Al_2Si_2O_5(OH)_4$ molar volume[b]: 98.56 - 99.34 cm³/mol
plagioclase (albite)[a] $Na_{0.74}Ca_{0.25}K_{0.016}Al_{1.25}Si_{2.75}O_8$ molar volume[b]: 100.07 cm³/mol	→	**kaolinite** $Al_2Si_2O_5(OH)_4$ molar volume[b]: 98.56 - 99.34 cm³/mol **gibbsite** $Al(OH)_3$ molar volume[b]: 31.96 cm³/mol

The mineral specific molar volumes of the educts and products and their chemical compositions depict where negative or positive volume budgets and element import or removal can occur.

[a] mineral composition determined by electron microprobe analyses (see Appendix A: Electronic Annex).

[b] molar volumes from Robie and Hemingway (1995).

[c] molar volumes depend on the hydration state and must be higher than the biotite molar volume (*e.g.*, a molar volume of 577 m³/mol is reported for illite in Robie and Hemingway (1995)).

Table 8 Parameters for O_2 depth profile calculations.

[Fe] average rock	24,872	ppm
[Zr] average rock	226	ppm
Fe(II) / Fe_{total} zone 4c	0.68	
Fe(II) / Fe_{total} zone 1	0.95	
mol O_2 used	0.25	mol
mol H_2O used	0.75	mol
n Fe	0.056	kg/mol
corestone zone thickness	3	m
rock density	2.675	kg/m^3
rock porosity	0.1	
O_2 atmosphere	9.02	mol O_2/m^3
profile depth	8.3	m

Zr and Fe concentrations, the profile depth, and the corestone zone thickness are from Hewawasam et al. (2013). Fe(II) / Fe_{total} ratios are from table 1. The rock density and the porosity are inferred from the He-pycnometry measurements. For calculation purposes, the O_2 concentration is converted from mol O_2/mol air into mol O_2/m^3 air.

Electronic Annex: Supplementary material

to

Mineralogical transformations set slow weathering rates in low-porosity metamorphic bedrock on mountain slopes in a tropical climate

by
Ricarda Behrens, Julien Bouchez, Jan A. Schuessler, Stefan Dultz,
Tilak Hewawasam, Friedhelm von Blanckenburg

published in Chemical Geology (2015)

Electron microprobe analyses

Electron microprobe analyses on primary minerals were done on four polished thin sections, which together represent the whole corestone weathering sequence. The measurements were performed with a JEOL JXA 8500F field emission electron probe micro analyzer at GFZ Potsdam. Multi element measurements (beam size 0.04 – 20 µm) were carried out on unweathered parts in pyroxene, biotite and plagioclase grains from corestone zone 1 to zone 4. The microprobe is equipped with 5 spectrometers and a Schottky-field emitter as electron gun. It was operated at 20 kV accelerating voltage and 20 nA beam current in WDS mode (wavelength dispersive spectra). The beam diameter was 1 µm (pyroxene), 5 µm (biotite), and 10 µm (plagioclase). The detection limit is 40 – 215 ppm (Ca and Ti, respectively). Peak counting times were 20 – 30 s, and background counting times were always set to half of the respective peak counting times. The CITZAF routine in the JEOL software, which is based on the Φ(ρZ) method (Armstrong, 1995), was used as matrix correction algorithm. The relative 2SD for major constituents of the minerals is <5.5%, and for minor components <38% (except for Na in biotite with 75% 2SD).

Plagioclase

Element-oxides in weight %, mean concentration data given for each corestone zone (Z1 to Z4)

	Sample-1-Z1, n=13	Sample-2-Z2, n=10	Sample-3-Z3, n=13	Sample-3-Z4a, n=5	Sample-5-Z4c, n=6
SiO_2	61.81	61.80	61.91	61.21	60.90
TiO_2	0.02	0.01	0.02	0.01	0.02
Al_2O_3	23.54	23.65	23.79	23.82	23.59
Cr_2O_3	d. l. *	d. l. *	d. l. *	d. l. *	d. l. *
SrO	d. l. *	d. l. *	d. l. *	d. l. *	d. l. *
FeO	0.08	0.05	0.06	0.05	0.05
MnO	0.01	0.01	0.01	d. l. *	0.01
MgO	d. l. *	d. l. *	d. l. *	d. l. *	d. l. *
CaO	5.27	5.25	5.31	5.18	5.21
Na_2O	8.45	8.57	8.50	8.61	8.48
K_2O	0.27	0.24	0.27	0.26	0.35
Cl	d. l. *	d. l. *	d. l. *	d. l. *	d. l. *
Total	99.45	99.57	99.86	99.13	98.60

d. l. *: below detection limit

Molar chemical formula based on O = 8				
Si	**Al**	**Ca**	**Na**	**K**
2.75	**1.25**	**0.25**	**0.74**	**0.02**

$(Na_{0.74}Ca_{0.25}K_{0.02})Al_{1.25}Si_{2.75}O_8$

Pyroxene

Element-oxides in weight %, mean concentration data given for each corestone zone (Z1 to Z4)

	Sample-1-Z1, n =20	Sample-2-Z2, n=20	Sample-3-Z3, n=23	sample-3-Z4a, n=5	Sample-5-Z4c, n=7
SiO_2	50.56	50.57	50.64	50.65	50.28
TiO_2	0.08	0.08	0.07	0.05	0.08
Al_2O_3	0.62	0.62	0.61	0.62	0.79
Cr_2O_3	0.01	0.01	0.01	d. l. *	0.01
SrO	d. l. *	d. l. *	d. l. *	d. l. *	d. l. *
FeO	33.19	33.36	33.13	33.34	33.53
MnO	0.65	0.62	0.60	0.62	0.57
MgO	14.45	14.24	14.56	14.30	14.18
CaO	0.53	0.52	0.49	0.47	0.47
Na_2O	0.01	0.02	0.02	0.02	0.02
K_2O	d. l. *	d. l. *	0.01	d. l. *	0.01
Cl	d. l. *	d. l. *	d. l. *	d. l. *	d. l. *
Total	100.09	100.09	100.14	100.07	99.94

d. l. *: below detection limit

Molar chemical formula based on O = 6					
Si	**Al**	**Fe**	**Mn**	**Mg**	**Ca**
1.97	**0.03**	**1.09**	**0.02**	**0.83**	**0.08**

$(Fe_{1.09}Mg_{0.83}Ca_{0.08}Al_{0.03}Mn_{0.02})Si_{1.97}O_6$

Biotite

Element-oxides in weight %, mean concentration data given for each corestone zone (Z1 to Z4)

	Sample-1-Z1, n=18	**Sample-2-Z2, n=15**	**Sample-3-Z2, n=7**	**Sample-3-Z3, n=11**	**Sample-3-Z4a, n=6**	**Sample-5-Z4c, n=6**
SiO_2	37.45	37.42	37.53	37.25	37.18	37.39
TiO_2	5.69	5.31	5.80	5.16	5.25	5.46
Al_2O_3	13.58	13.68	13.78	13.94	13.86	13.75
Cr_2O_3	d. l. *	d. l. *	d. l. *	d. l. *	d. l. *	d. l. *
SrO	0.13	0.14	0.14	0.13	0.13	0.13
FeO	19.63	19.77	19.42	19.94	19.73	19.94
MnO	0.08	0.07	0.07	0.06	0.05	0.06
MgO	10.88	11.16	11.03	11.39	11.21	10.84
CaO	d. l. *	d. l. *	d. l. *	d. l. *	d. l. *	d. l. *
Na_2O	0.06	0.04	0.05	0.07	0.06	0.09
K_2O	9.13	9.19	9.15	9.01	9.16	9.28
Cl	0.11	0.11	0.11	0.11	0.11	0.11
Total	96.75	96.89	97.07	97.08	96.75	97.04

d. l. *: below detection limit

Molar chemical formula based on O = 12								
Si	**Ti**	**Al**	**Sr**	**Fe**	**Mg**	**Na**	**K**	**Cl**
3.06	**0.34**	**1.33**	**0.01**	**1.35**	**1.35**	**0.01**	**0.96**	**0.02**

$(K_{0.96}Na_{0.01})(Fe_{1.35}Mg_{1.35}Ti_{0.34}Sr_{0.01})(Al_{1.33}Si_{3.06})O_{10}((OH)_2Cl_{0.02})$

Calculation of the parameters for the oxidation model (section 4.2.1)

All parameters required to calculate the volume increase by oxidation of iron-bearing minerals in the bedrock, equation (5) in the main text, are presented below. In the following equations each occurrence of "x" can be replaced either by "bt" for biotite or "px" for pyroxene.

We first need to calculate the total amount of FeO lost during weathering between bedrock and the weathered zone j in the corestone, $FeO_{lost,\,j}$ (in moles/kg_{rock}):

$$FeO_{lost,j} = \left(\left([px]_0 - [px]_j\right) * [FeO]_{px} + \left([bt]_0 - [bt]_j\right) * [FeO]_{bt}\right) * \frac{1}{M_{FeO}} \qquad \text{(S1)}$$

Where $[x]_0$ and $[x]_j$ is the concentration of mineral x (kg_x/kg_{rock}) in the bedrock and corestone zone j, respectively (obtained by point-counting and CIPW norm calculation by Hewawasam et al. 2013"). $[FeO]_x$ is the concentration of FeO in mineral x (kg/kg_x), obtained from microprobe measurements (tables above), and M_{FeO} is the molar mass of FeO (kg/mol).

The amount of Fe-bearing mineral in the rock $[x]_0$ is obtained by multiplying the concentration of the mineral in the rock (vol%) with the density of the mineral ρ_x (kg/m^3) divided by the density of the rock ρ_{rock} (kg/m^3):

$$[x]_0 = [x]_{rock} * \frac{\rho_x}{\rho_{rock}} \qquad \text{(S2)}$$

The density of the minerals is taken from literature (Table 4 in the main text, (Robie and Hemingway, 1995)), and the rock density was calculated from the weighed cylinders prepared for He-pycnometry measurements.

As the degree of mineral weathering is comparable to the amount of *in situ* Fe oxidation in the mineral, the amount of the weathered mineral in corestone zone j is evaluated using the mass transfer coefficient ($\tau_{x,\,j}$, Table 5, main text) from Hewawasam et al. (2013). For pyroxene we used τ_{Mn} since nearly all Mn is incorporated in pyroxene. This assumption introduces negligible uncertainties into the full calculation. Biotite depletion τ_{bt} was determined using the biotite loss in the different corestone zones as calculated from Sr isotopes (Hewawasam et al., 2013). Therefore, equation (S1) becomes:

$$FeO_{lost,j} = \left([px]_0 * [FeO]_{px} * \left(-\tau_{px,j}\right) + [bt]_0 * [FeO]_{bt} * \left(-\tau_{bt,j}\right)\right) * \frac{1}{M_{FeO}} \qquad \text{(S3)}$$

In addition to the amount of Fe(II) lost during weathering, the amount of Fe(III) formed during weathering is needed for this calculation (see below). As Fe is immobile in the corestone (τ_{Fe} = 0), $FeO_{lost,\,j}$ (mol/kg_{rock}) must equal the amount of $Fe(OH)_3$ (mol/kg_{rock}) formed during weathering

$$FeO_{lost,j} = Fe(OH)_{3},_{j} \qquad \text{(S4)}$$

hence the concentration of $[Fe(OH)_3]_j$ in corestone zone j (kg/kg_{rock}) is:

$$[Fe(OH)_3]_j = FeO_{lost,j} * M_{Fe(OH)_3} \qquad \text{(S5)}$$

Where $M_{Fe(OH)3}$ is the molar mass of $Fe(OH)_3$ (kg/mol).

The Fe contained in pyroxene and biotite $[Fe]_x$ (kg/kg_{rock}) with respect to the whole rock is obtained by multiplying the concentration of the mineral (kg/kg_{rock}) with the concentration of FeO in the mineral $[FeO]_x$ (kg/kg_x):

$$[Fe]_X = [x]_0 * [FeO]_X \qquad \text{(S6)}$$

To derive a value for the fracture criterion for a given layer of our weathering system, we rewrite the elastic strain equation from Fletcher et al. (2006), where the physical change is related to chemical reaction advance:

$$\varepsilon = \frac{\xi f_0}{3} * \left[\frac{V_{Fe(OH)_3} - V_{FeO}}{V_{FeO}}\right] \qquad \text{(S7)}$$

To equation (4) in the main text (section 4.2.1).

Worked example for the oxidation model (section 4.2.1)

The parameter for the oxidation model calculations are given in Table 3, main text. Note that we have not included the subscript of the enumerator in the table, but included them in the detailed calculation

for the worked sample. The calculation for biotite is worked out for an annite like composition and the max. biotite weathering rate, as given in Hewawasam et al. (2013). The same calculation was done for phlogopite and the min. weathering rate, too. To derive the amount of Fe-bearing mineral in the rock $[x]_0$, we insert the given values in equation (S2) which yield:

$$[px]_0 = 0.04\, {m^3}_{px}/{m^3}_{rock} * \frac{3998\ {kg_{px}/m^3}_{px}}{2700\ kg_{rock}/{m^3}_{rock}} = \mathbf{0.059\ kg_{px}/kg_{rock}}$$

$$[bt]_0 = 0.07\ {m^3}_{bt}/{m^3}_{rock} * \frac{3317\ {kg_{bt}/m^3}_{bt}}{2700\ kg_{rock}/{m^3}_{rock}} = \mathbf{0.086\ kg_{bt}/kg_{rock}}$$

Calculating the Fe contained in pyroxene and biotite $[Fe]_x$ (kg/kg_{rock}) with equation (S6) gives:

$$[Fe]_{px} = 0.059\ kg_{px}/kg_{rock} * 0.33\, kg_{FeO}/kg_{px} = \mathbf{0.020\, kg_{FeO}/kg_{rock}}$$

$$[Fe]_{bt} = 0.086\ kg_{bt}/kg_{rock} * 0.200\, kg_{FeO}/kg_{bt} = \mathbf{0.017\, kg_{FeO}/kg_{rock}}$$

Therefore, *e.g.* in corestone zone 3 $FeO_{lost,\,j}$ becomes (S3):

$$FeO_{lost,j} = \Big(0.059\ kg_{px}/kg_{rock} * 0.33\, kg_{FeO}/kg_{px} * (-0.30) + 0.086\ kg_{bt}/kg_{rock} * 0.200\, kg_{FeO}/kg_{bt} * (-0.13)\Big) * \frac{1}{0.069\, kg/mol}$$

$$= \mathbf{1.17 * 10^{-1}\, mol/kg_{rock}}$$

As this is equal to $[Fe(OH)_3]_j$ we can insert this into equation (S5):

$$[Fe(OH)_3]_j = 1.17 * 10^{-1}\, mol/kg_{rock} * 0.107\, kg/mol = \mathbf{1.25 * 10^{-2}\, kg/kg_{rock}}$$

With these values we can calculate $\Delta\tilde{V}$, equation (5) from the main text:

$$\Delta\tilde{V} = V_{FeO} * \big([Fe]_{bt,0} * (1 + \tau_{bt,j}) - [Fe]_{bt,0}\big) + V_{FeO} * \big([Fe]_{px,0} * (1 + \tau_{px,j}) - [Fe]_{px,0}\big) + V_{Fe(OH)_3} * \big([Fe(OH)_3]_j - [Fe(OH)_3]_0\big)$$

$$\Delta\tilde{V} = 1.75 * 10^{-4}\, m^3/kg * (0.017\, kg_{FeO}/kg_{rock} * (1 + (-0.13)) - 0.017\, kg_{FeO}/kg_{rock}) + 1.75 * 10^{-4}\, m^3/kg * (0.020\, kg_{FeO}/kg_{rock} * (1 + (-0.30)) - 0.020\, kg_{FeO}/kg_{rock}) + 1.92 * 10^{-4}\, m^3/kg * (1.25 * 10^{-2}\, kg/kg_{rock} - 0\, kg/kg_{rock})$$

$$= \mathbf{9.90 * 10^{-7}\, m^3/kg_{rock}}$$

For the elastic strain this reveals (equation (4) in the main text):

$$\varepsilon = \frac{1}{3} * \Delta\tilde{V} * \rho_{rock}$$

$$\varepsilon = \frac{1}{3} * 9.90 * 10^{-7}\, m^3/kg_{rock} * 2700\ kg_{rock}/{m^3}_{rock}$$

$$= \mathbf{8.91 * 10^{-4}}$$

Inserting this into equation (3) from the main text:

$$2\Gamma = \frac{E\varepsilon^2}{1-\nu} = U$$

$$U = \frac{1 * 10^{12}\, dyn/cm^2 * (8.91 * 10^{-4})^2}{1 - 0.25} = \mathbf{1.06 * 10^6\, dyn/cm^2}$$

This shows that already in zone 3 the fracturing criterion:

$2\Gamma = 4.0 * 10^5\, dyn/cm^2 < U$ is reached

References

Armstrong, J.T., 1995. CITZAF - A package of correction programs for the quantitative electron microbeam X-ray-analysis of thick polished materials, thin films, and particles. Microbeam Analyses 4, 177-200.

Fletcher, R., Buss, H., Brantley, S., 2006. A spheroidal weathering model coupling porewater chemistry to soil thicknesses during steady-state denudation. Earth and Planetary Science Letters 244, 444-457.

Hewawasam, T., von Blanckenburg, F., Bouchez, J., Dixon, J.L., Schuessler, J.A., Maekeler, R., 2013. Slow advance of the weathering front during deep, supply-limited saprolite formation in the tropical Highlands of Sri Lanka. Geochimica et Cosmochimica Acta 118, 202-230.

Robie, R.A., Hemingway, B.S., 1995. Thermodynamic Properties of Minerals and Related Substances at 298.15 K and 1 Bar (10^5 Pascals) Pressure and at Higher Temperatures. U. S. Geological Survey Bulletin, Washington.